



HAL
open science

Transition Metal Dichalcogenide TiS₂ Prepared by Hybrid Atomic Layer Deposition/Molecular Layer Deposition: Atomic-Level Insights with In Situ Synchrotron X-ray Studies and Molecular Surface Chemistry

P. Younes, E. Skopin, M. Zhukush, L. Rapenne, H. Roussel, N. Aubert, L. Khrouz, C. Licitra, C. Camp, Marie-Ingrid Richard, et al.

► **To cite this version:**

P. Younes, E. Skopin, M. Zhukush, L. Rapenne, H. Roussel, et al.. Transition Metal Dichalcogenide TiS₂ Prepared by Hybrid Atomic Layer Deposition/Molecular Layer Deposition: Atomic-Level Insights with In Situ Synchrotron X-ray Studies and Molecular Surface Chemistry. *Chemistry of Materials*, 2022, 34 (24), pp.10885-10901. 10.1021/acs.chemmater.2c02369 . hal-03937100

HAL Id: hal-03937100

<https://hal.science/hal-03937100>

Submitted on 31 Oct 2023

HAL is a multi-disciplinary open access archive for the deposit and dissemination of scientific research documents, whether they are published or not. The documents may come from teaching and research institutions in France or abroad, or from public or private research centers.

L'archive ouverte pluridisciplinaire **HAL**, est destinée au dépôt et à la diffusion de documents scientifiques de niveau recherche, publiés ou non, émanant des établissements d'enseignement et de recherche français ou étrangers, des laboratoires publics ou privés.

This document is confidential and is proprietary to the American Chemical Society and its authors. Do not copy or disclose without written permission. If you have received this item in error, notify the sender and delete all copies.

Transition Metal Dichalcogenide TiS₂ Prepared by Hybrid Atomic Layer Deposition/Molecular Layer Deposition: Atomic-Level Insights With in situ Synchrotron X-ray Studies And Molecular Surface Chemistry.

Journal:	<i>Chemistry of Materials</i>
Manuscript ID	cm-2022-02369w.R1
Manuscript Type:	Article
Date Submitted by the Author:	n/a
Complete List of Authors:	ABI YOUNES, Petros; Universite Grenoble Alpes, Skopin, Evgeniy ; Laboratoire des technologies de la microelectronique Zhukush, Medet; IRCELYON Rapenne, Laetitia; Institut Polytechnique de Grenoble, of Materials Science Roussel, Hervé; Universite Grenoble Alpes, LMGP Aubert, Nicolas; Synchrotron SOLEIL - Beamline SIRIUS, Khrouz, Lhossain; Ecole normale superieure de Lyon, Laboratoire de Chimie Licitra, Christophe; CEA-Leti CAMP, Clément; C2P2, Richard, Marie-Ingrid; ESRF, Schneider, Nathanaelle; IPVF Ciatto, Gianluca; Synchrotron SOLEIL, experience Gauthier, Nicolas; CEA-Leti Rouchon, Denis; CEA-Leti Quadrelli, Elsje; IRCELYON Renevier, Hubert; Universite Grenoble Alpes, Laboratoire des Matériaux et du Génie Physique, UMR 5628

SCHOLARONE™
Manuscripts

1
2
3
4 **Transition Metal Dichalcogenide TiS₂ Prepared by Hybrid**
5 **Atomic Layer Deposition/Molecular Layer Deposition:**
6 **Atomic-Level Insights With *in situ* Synchrotron X-ray**
7 **Studies And Molecular Surface Chemistry.**
8
9
10
11
12

13 Petros Abi Younes^{1,2,*}, Evgeniy Skopin¹, Medet Zhukush³, Laetitia Rapenne¹, Hervé
14 Roussel¹, Nicolas Aubert⁵, Lhoussain Khrouz⁶, Christophe Licitra², Clément Camp⁴,
15 Marie-Ingrid Richard^{7,8}, Nathanaelle Schneider,⁹ Gianluca Ciatto⁵, Nicolas
16 Gauthier², Denis Rouchon,² Elsje Alessandra Quadrelli^{3,*} and Hubert Renevier^{1, *}
17
18
19

20 ¹*LMGP, Univ. Grenoble Alpes, CNRS, Grenoble-INP, Grenoble, France*

21 ²*Univ. Grenoble Alpes, CEA, LETI, F-38000 Grenoble, France*

22 ³*Université de Lyon, IRCELYON, Institut de Recherche sur la catalyse et l'environnement (UMR*
23 *5256 CNRS Université Lyon1), 2 av. Albert EINSTEIN, 69100 Villeurbanne, France*

24 ⁴*Université de Lyon, CP2M, Laboratory of Catalysis, Polymerization, Processes and Materials,*
25 *UMR 5128 CNRS-UCB Lyon 1-CPE Lyon, Institut de Chimie de Lyon, 43 Bvd du 11 Novembre*
26 *1918, 69616 Villeurbanne, France*

27 ⁵*Synchrotron SOLEIL, Beamline SIRIUS, L'Orme des Merisiers, Saint-Aubin, F-91192, Gif sur*
28 *Yvette, France*

29 ⁶*ENSL, CNRS, Laboratoire de Chimie UMR 5182, ENS Lyon (École Normale Supérieure de Lyon,*
30 *site René Descartes), 15 parvis René Descartes, 69342 Lyon, France*

31 ⁷*Univ. Grenoble Alpes, CEA Grenoble, IRIG, MEM, NRS, 17 rue des Martyrs 38000 Grenoble,*
32 *France*

33 ⁸*European Synchrotron Radiation Facility, 71 Avenue des Martyrs, 38043 Grenoble, France*

34 ⁹*IPVF (UMR 9006), Institut Photovoltaïque d'Ile-de-France, 18 boulevard Thomas Gobert,*
35 *91120 Palaiseau, France*

36 * *petros.abi-younes@grenoble-inp.fr ; * elsje.quadrelli@ircelyon.univ-lyon1.fr ; **
37 *hubert.renevier@grenoble-inp.fr*

38
39
40
41
42
43
44
45
46
47
48
49
50
51
52
53
54
55
56
57
58
59
60
23/10/2022 21:26

Abstract

In this work, 2D-material titanium disulfide (TiS_2) film was grown using tetrakis(dimethylamido)titanium and 1,2 ethanedithiol on 100 nm thick amorphous SiO_2/Si substrate. The first step of the process relied on the growth of an amorphous film of Ti amidothiolate by hybrid Atomic Layer Deposition/Molecular Layer Deposition (ALD/MLD) at 50 °C. Such thiolate converted into TiS_2 upon subsequent thermal annealing under $\text{H}_2(4\%)/\text{Ar}(96\%)$ at 450 °C. The final lamellar TiS_2 layers tend to be parallel to the substrate surface as observed by transmission electron microscopy and confirmed at a larger scale by x-ray absorption linear dichroism at the Ti K-edge. The crystalline quality of the resulting films was assessed by Raman scattering. Angle-resolved x-ray photoelectron spectroscopy and hard x-ray photoelectron spectroscopy confirmed the stoichiometry of the TiS_2 layer.

Repetitive and self-limiting growth behavior on the SiO_2/Si substrate was displayed from the early stages of the growth using *in situ* synchrotron radiation yielding the Ti and S x-ray fluorescence, *in situ* ellipsometry and x-ray reflectivity. Modeling the initial ALD and MLD half-cycles on high-surface-area silica beads afforded characterization by more analytical techniques and provided insights to the growth chemistry that agreed with observations on SiO_2/Si substrate.

Four-point probe resistivity measurements and spectroscopic ellipsometry strongly suggest that the thin films grown on SiO_2/Si substrates behave as heavily doped semiconductors.

1. Introduction

2D-materials, especially Transition Metal Dichalcogenides (TMDC)¹, have received considerable attention recently since emerging as a class of exceptional materials with many potential applications (supercapacitors, batteries, electronics and optoelectronics, flexible electronics, ...) ²⁻⁴. TMDCs show unique thickness-dependent properties such as the modulation of the bandgap transition value with the number of 2D layers.⁵ Titanium disulfide, TiS₂, which consists of S-Ti-S layers separated by van der Waals gaps, is among the several interesting lamellar TMDC to be investigated for emerging devices: thin TiS₂ is more efficient than bulk material for new supercapacitor electrodes,⁶ for low resistivity layered materials enabling the formation of intercalation compounds for rechargeable batteries⁷, or as new hybrid TiS₂-based material to be deposited with organic intercalation^{8,9}. The TiS₂ layer number/thickness, along with its stoichiometry critically define its semimetal or semiconductor nature¹⁰.

To date, most investigations of TMDC, there included TiS₂, are performed on flakes produced by mechanical exfoliation of bulk crystals. As these are not suited for large-scale applications, methods to deposit uniform high-quality films of accurately controlled thickness on large area are needed to allow full deployment of TMDC materials. While most strategies are based on Chemical Vapor Deposition (CVD), Physical Vapor Deposition (PVD) methods, or chalcogenization of metal or metal oxides,^{11,12} Atomic Layer Deposition (ALD) - a gas-phase deposition technique based on sequential, self-limiting surface reactions - appears better adapted to obtain conformal film growth with precise thickness level control, good reproducibility and homogeneity over the substrate area.¹³ ALD is already used to

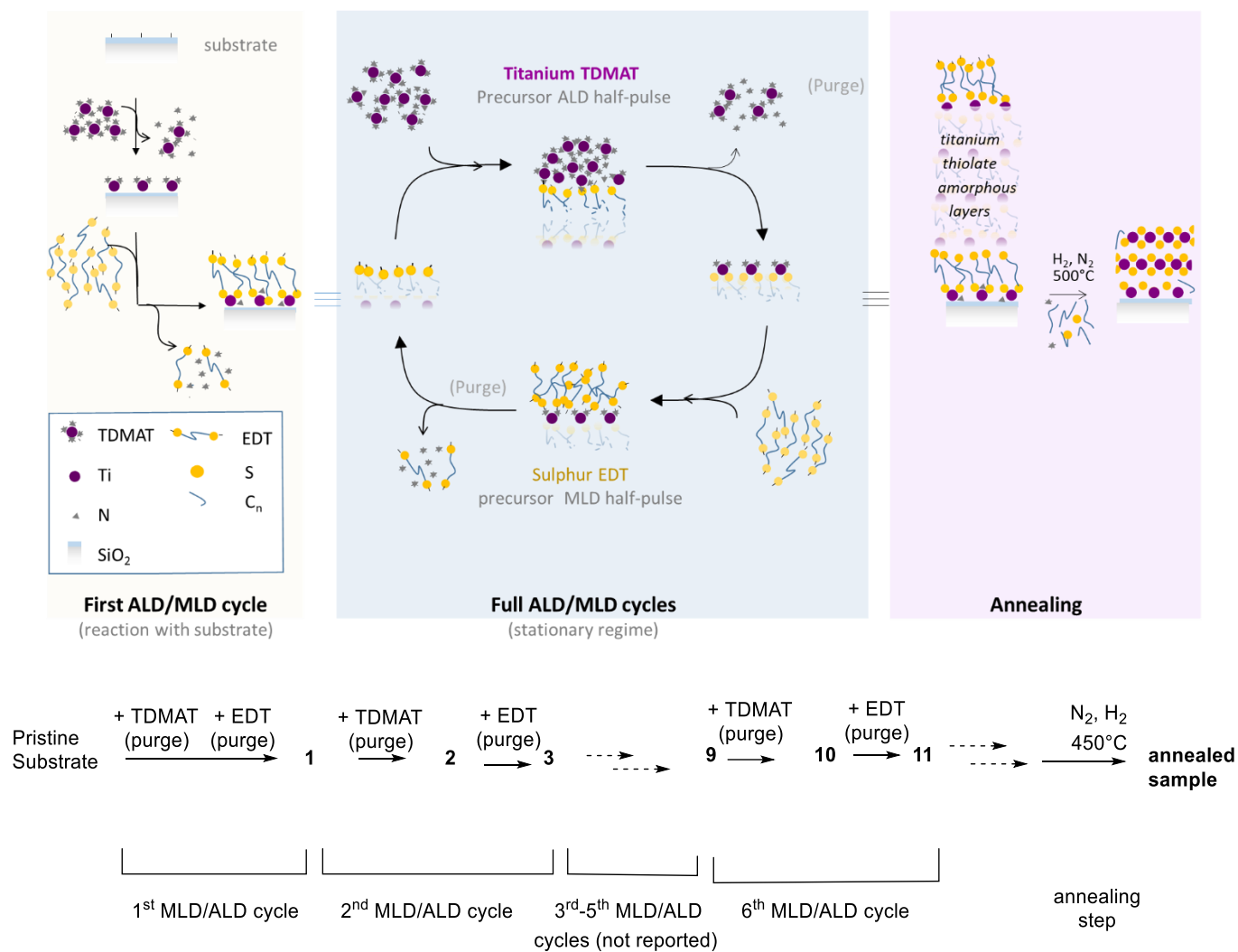
1
2
3 deposit ultrathin films, but the anisotropy of TMDC coupled with the extreme
4 thinness required brings about new challenges, and despite several efforts, the
5 deposition of as-deposited crystalline TMDC remains difficult, possibly necessitating
6 post-annealing steps or chalcogenization of ALD-grown transition metal oxides.^{14–}
7
8
9
10
11
12 ¹⁸Among the complicating factors is the co-occurrence of growth and crystallization
13 during the ALD process which becomes particularly limiting when a pre-determined
14 crystal orientation is required. The use of specific crystalline substrates with
15 adequate lattice parameters is a possible strategy to overcome this latter problem.
16 Another approach, which has a larger substrate scope, and is presented herein, is
17 to completely dissociate deposition and crystallization. Such possibility can be
18 accessed by combining the use of organic precursors during the ALD process (such
19 as for example, alcohols, ROH -R being a generic organic fragment- rather than H₂O
20 as oxygen source). The presence of the organic chemical residues prevents the
21 crystallization during the growth of the hybrid inorganic-organic thin film
22 (metalcones in the examples just mentioned ^{13,19}) at low temperatures. A
23 subsequent treatment (typically annealing which induces loss of most of the organic
24 fragment) leads to the crystallization of the mineral phase.^{20,21} For instance, the
25 combination of such organic precursor-based ALD approach — which is called
26 herein Atomic Layer deposition/Molecular Layer Deposition (ALD/MLD)¹⁹ — and
27 post-annealing step allowed to control the porosity of Al₂O₃ thin films,²² as well as
28 the crystallinity, composition, and electrochemical properties of SnO/SnO₂,²³ TiO₂,
29 and V₂O₅.²⁴ In the field of TMDC, the authors have demonstrated the value of
30 replacing H₂S, the usual molecule used for sulfide phases growth by ALD, with the
31 MLD precursor 1,2-ethanedithiol (EDT, HSCH₂CH₂SH) to obtain, after annealing,
32 atomically thin MoS₂- based layers oriented parallel the substrate,²⁵ with residual
33
34
35
36
37
38
39
40
41
42
43
44
45
46
47
48
49
50
51
52
53
54
55
56
57
58
59
60

1
2
3 carbon content similar to an organic precursor-free plasma-enhanced-ALD (PE-ALD)
4 process to MoS₂.
5
6
7

8 The material of interest here is TiS₂. In the literature, TiS₂ has been
9 synthesized by different growth techniques such as Chemical Vapor Deposition
10 (CVD),^{26–31} chemical exfoliation method³², wet chemical synthesis³³, and the ALD
11 reports remain scant.^{2,7,33–37} The first ALD growth of TiS₂, reported in 2007 by Pore
12 *et al.*, was grown from TiCl₄ and H₂S as titanium and sulphur precursors.⁷ Since then,
13 alternative Ti (tetrakis(dimethylamido)titanium, TDMAT)³⁵ and S (H₂S plasma)³⁸
14 sources have been considered as well as two-step strategy (sulfurization of PEALD-
15 TiN thin films).³⁷ In all cases, the material growth and properties appear strongly
16 dependent on the nature of the substrate and no high-quality ultrathin layered
17 materials could be obtained.^{2,7,34–36} Besides, only few applications of ALD TiS₂ thin
18 films are reported (photo-harvesting material, Li⁺/Na⁺ intercalation, CO₂ reduction
19 reaction), and the challenge of producing ultrathin lamellar TiS₂ remains.
20
21
22
23
24
25
26
27
28
29
30
31
32
33

34 Herein, we consider a novel approach to generate ultrathin lamellar TiS₂-
35 based thin films even on a non-epitaxial substrates such as thermal silicon oxide,
36 which is widely used in microelectronics. The novel approach corresponds to
37 combining an ALD step from TDMAT with a MLD step from EDT (as a safer
38 alternative to highly toxic H₂S) to generate an amorphous hybrid organic-inorganic
39 Ti-thiolate material, with a subsequent annealing treatment at a mild temperature
40 (lower than 450 °C), which leads to a successful in-plane crystallization (see **Scheme**
41 **1**). The self-limiting nature of the surface reactions that are necessary to ensure the
42 uniformity, conformality, scalability, and repeatability of the process, are assessed
43 by several advanced techniques coupling, *inter alia*, *in situ* X-ray based monitoring
44
45
46
47
48
49
50
51
52
53
54
55
56
57
58
59
60

1
2
3 of the process and chemical modeling on high-surface area silica that collectively
4
5 lead to a deep understanding of the process.
6
7
8
9
10
11
12
13
14
15
16
17
18
19
20
21
22
23
24
25
26
27
28
29
30
31
32
33
34
35
36
37
38
39
40
41
42
43
44
45
46
47
48
49
50
51
52
53
54
55
56
57
58
59
60



Scheme 1: Schematic overview of the ALD/MLD step (blue background) and annealing step (pink background) of the overall process to TiS₂ reported here and numbering scheme adopted for the silica-supported solids of the modeling studies.

2. Experiments

2.1. Starting chemicals

Tetrakis(dimethylamido)titanium (IV), TDMAT (CAS number: 3275-24-9, 99.999% purity) and ethylenedithiol, EDT (CAS number: 540-63-6, assay greater than 99%) were purchased from Merck™. The reference TiS₂ sample was purchased from Merck™ (CAS number: [12039-13-3]). All reactions among molecular precursors or between molecular precursors and silica beads were carried out under a controlled argon atmosphere using Schlenk glassware and glovebox. General preparing procedure and materials as well as equipment are detailed in the Supplementary Information (SI).

2.2. Modeling of ALD/MLD growth on silica-terminated silicon wafers by surface chemistry on silica nanobeads

Chemical experimental modeling on high surface area silica beads is explored to identify the appropriateness of the chosen precursors to lead to molecularly-precise ALD/MLD cycles. Selected growth steps of the proposed ALD/MLD process (see **scheme 1**) were carried out on silica nanobeads as a substrate (loose powder, 200 m²/g), following an experimental molecular modeling strategy outlined elsewhere.²⁵

1
2
3 1 Silica was treated at 700 °C under dynamic vacuum before ALD/MLD cycles (see
4
5 2 SI for further details on the silica beads pre-treatment procedure). Between each
6
7 3 half-cycle (that is a reactant pulse followed by the purge step), modified silica beds
8
9 4 were sampled and stored separately in an argon-filled glovebox for elemental
10
11 5 analyses, to determine chemical composition, and for spectroscopic analyses by
12
13 6 infrared and solid-state Nuclear Magnetic Resonance (NMR).
14
15

16
17 7 *TDMAT pulses:* The TDMAT pulses were performed by connecting the TDMAT-
18
19 8 containing bulb to the glass-tube containing the silica-based powder substrate
20
21 9 under static vacuum (typically 10^{-5} Torr). The glass-tube under vapor pressure of
22
23 10 TMDAT was then closed and placed in an oven at 70 °C for 4.5 hours. The glass-
24
25 11 reactor was shaken every 30 minutes to facilitate the homogeneous exposure of
26
27 12 the silica beads to the vapor. During the first pulse, the white silica-beads turned
28
29 13 pale yellow.
30
31

32 14 *EDT pulses:* The EDT-containing flask was connected to the glass-tube containing
33
34 15 the substrate under static Ultra-High Vacuum (UHV) at room temperature. After
35
36 16 closure of the valve, the glass-tube was left under vapor pressure of EDT for 20
37
38 17 minutes at room temperature. For the first cycle, upon reaction with EDT, the
39
40 18 powder gradually changed color from yellow to red. The glass-reactor was shaken
41
42 19 every 5-10 minutes to homogenize the powder.
43
44

45
46 20 *Purge steps:* The purge steps were carried out to remove excess precursor
47
48 21 vapors and by-products from the substrate after each TDMAT or EDT pulse. The
49
50 22 steps were performed by placing the glass-tube under dynamic UHV for 30 minutes
51
52 23 while heated in a tubular oven at 70 °C.
53
54
55
56
57
58
59
60

1
2
3 1 *Analysis of the volatile by-products.* At the end of each pulse and before the
4
5 2 purge step, the volatiles were condensed in an NMR tube containing D₂O and MeOH
6
7 3 (as internal standard).
8
9

10 4 **2.3. ALD/MLD on silica-terminated silicon wafers and thermal annealing** 11 12 5 **conditions** 13 14

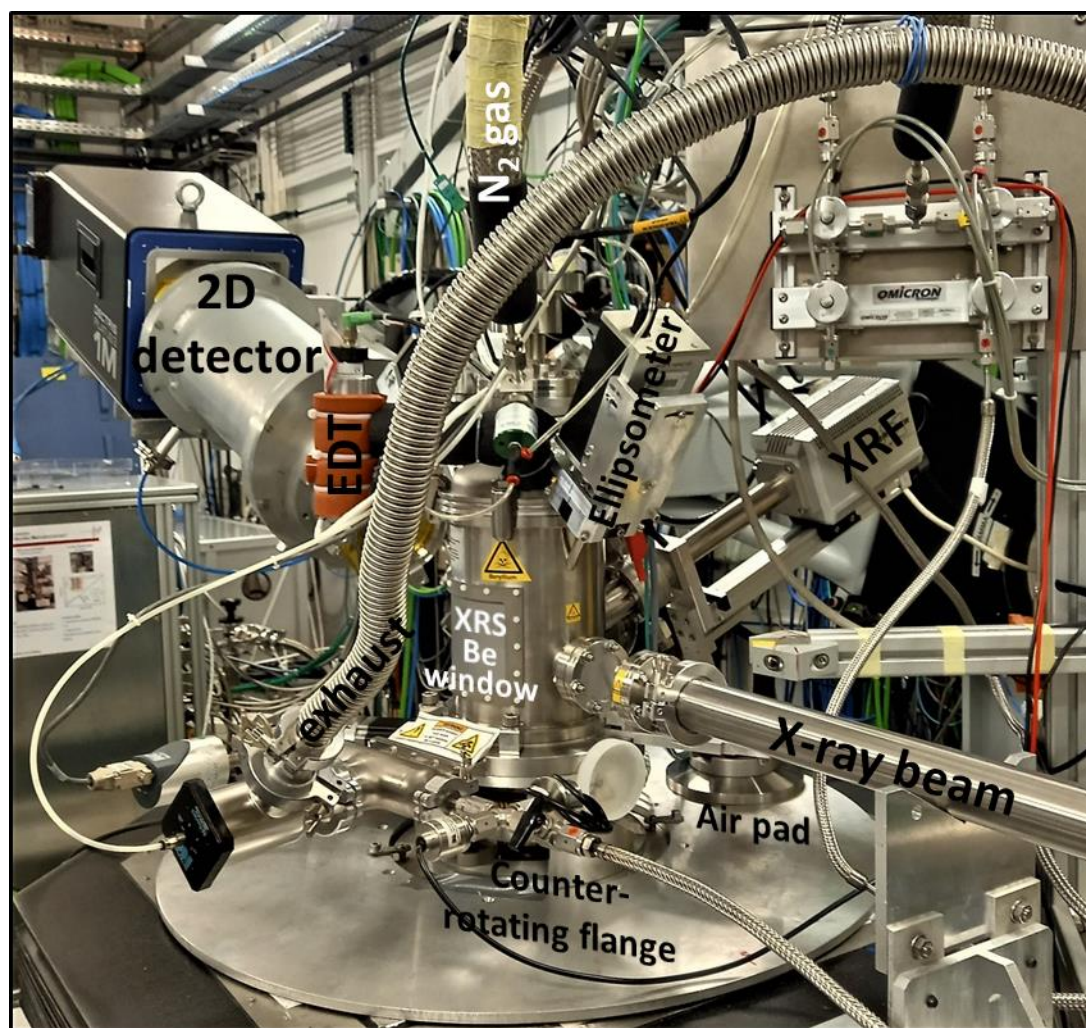
15 6 ALD/MLD experiments were performed on a 100 nm-thick thermally grown
16
17 7 amorphous SiO₂ layer on Si wafers (hereafter denoted 100 nm-SiO₂). Prior to
18
19 8 deposition, the substrate surface was pre-treated at 200 °C in a 100 sccm of N₂ flow
20
21 9 for 30 minutes. The sample holder temperature was 50°C during the ALD/MLD
22
23 10 growth. The pre-treated substrate was sequentially exposed to TDMAT. TDMAT was
24
25 11 carried by a 50 sccm flow of Ar gas. TDMAT/Ar bubbler was maintained at room
26
27 12 temperature (25 °C). EDT evaporator was heated at 40 °C to maintain enough
28
29 13 pressure value ($P_{EDT} = 12$ mbar at the beginning of the injection). Both precursors
30
31 14 were sequentially injected into a closed reactor chamber. Between each precursor
32
33 15 pulse, the reactor chamber was purged out with a 100 sccm flow of N₂ to remove
34
35 16 reaction by-products.
36
37
38

39 17 ALD/MLD growths of 40 or 80 cycles were followed by thermal annealing at 450 °C
40
41 18 for 30 min under 100 sccm flow of H₂(4%)/Ar(96%) with a ramp rate equal to 10
42
43 19 °C/min when increasing or decreasing the temperature.
44
45

46 20 **2.3.1. *In situ* characterization** 47 48

49 21 The two-step process on silica wafers -ALD/MLD followed by thermal annealing -,
50
51 22 was developed in a custom-built portable reactor which mounts onto the 6-axis
52
53 23 tower of the Newport™ diffractometer installed at the beamline SIRIUS³⁹ of SOLEIL
54
55 24 synchrotron facility (see **Figure 1**). The set-up allows to use a complementary suite
56
57
58
59
60

1
2
3 1 of *in situ* synchrotron x-ray techniques (reflectivity, grazing-incidence fluorescence,
4 diffraction, and absorption).⁴⁰ The SIRIUS beamline³⁹ has unique characteristics to
5 work in the tender x-ray range [1.2-5] keV, such as a variable-polarization HU36
6 undulator source and two monochromators. Experiments with the synchrotron
7 radiation were carried out with the direct Drive double Crystal Monochromator
8 (DCM), which allows both step and continuous energy scanning modes with high
9 energy resolution.
10
11
12
13
14
15
16
17
18
19
20
21
22
23
24
25
26
27
28
29
30
31
32
33
34
35
36
37
38
39
40
41
42
43
44
45
46
47
48
49
50
51
52
53



9
10 **Figure 1:** ALD/MLD reactor built for surface sensitive (grazing incidence) *in situ* synchrotron x-
11 ray studies, installed on the tower of the diffractometer of SIRIUS beamline (SOLEIL synchrotron).
54
55
56
57
58
59
60

1
2
3 1 As shown, the reactor has x-ray transparent windows for x-ray scattering (cylindrical 400 μm thick
4 2 beryllium window) and spectroscopy (20 μm thick Kapton foil) with the sample in horizontal
5 3 scattering geometry. The chamber maintains several ports for ALD gas injection, fluorescence and
6 4 optical measurements (ellipsometry).
7
8
9 5
10
11

12 6 Synchrotron radiation XRF and XRR have been performed *in situ* during the
13 7 sample growth and subsequent thermal annealing. A four-element Silicon Drift
14 8 Detector (SDD) manufactured by Bruker (XFlash QUAD 5040) was used to measure
15 9 the XRF and a 2D hybrid pixel detector (PILATUS 1M by Dectris) was used to
16 10 measure the XRR (and, incidentally, the x-ray scattering). The SDD was mounted on
17 11 a dedicated flange of the reactor which allows to optimize the sample-detector
18 12 distance; the detector nose (located into the reactor chamber) was equipped with
19 13 a collimator directed at the center of the sample surface and a 20 micron-thick
20 14 Kapton entrance window which separates the SDD from the chemicals in the
21 15 reactor. The four-element SDD was coupled to a four-channel xMAP DXP electronics
22 16 provided by XIA. For *in situ* reflected beam intensity measurement, the x-ray beam
23 17 energy was equal to 5 keV and the incident angle α_i was equal to 1.2° , that is above
24 18 the critical angle α_c for Si ($\alpha_c=0.35^\circ$ at 5 keV). For monitoring the Ti and S XRF yields,
25 19 the incoming x-ray beam energy was equal to 5 keV, i.e. above the Ti and S K-edges
26 20 (4966 and 2472 eV respectively).
27
28
29
30
31
32
33
34
35
36
37
38
39
40
41
42
43
44

45 21 ALD/MLD was monitored by *in situ* multi-wavelength ellipsometry (MWE), using a
46 22 4-wavelengths (465 nm, 525 nm, 580 nm, and 635 nm) Film Sense FS-1™ Banded
47 23 Wavelength Ellipsometer and FS-1 software for thickness calculation. The refractive
48 24 index as a function of wavelength of the Ti-thiolate could not be measured *ex situ*,
49 25 therefore we used the ellipsometry model for the calculation of TiO_2 film
50 26 thicknesses.⁴¹ Although the fit gave reasonable values during ALD/MLD, the latter
51
52
53
54
55
56
57
58
59
60

1
2
3 1 are not taken as definite in the present paper. The actual thicknesses were
4
5 2 measured by x-ray Reflectivity (XRR).
6
7

8 3 *In situ* x-ray Absorption Near-Edge structure Spectroscopy (XANES) at both
9
10 4 the Ti and S K-edges was performed in fluorescence detection mode using the four-
11
12 5 element SDD described above. The incident angle was 1.2°. All XANES experiments
13
14 6 were performed using a DCM monochromator equipped with Si (111) crystals, and
15
16 7 changing the beamline HU36 undulator gap simultaneously with the
17
18 8 monochromator Bragg angle during the continuous energy scan. A continuous
19
20 9 energy scanning mode was used, synchronizing the speed of monochromator and
21
22 10 undulator movements; this minimizes the acquisition deadtime and take spectra in
23
24 11 a faster way. For Ti K-edge XANES, a couple of Pt-coated mirrors were used in order
25
26 12 to reject high-order harmonics and focus the beam in vertical, while C-coated
27
28 13 mirrors were used for S K-edge XANES. Grazing incidence geometry was used for all
29
30 14 scans to limit the x-ray penetration in the substrate.
31
32
33

34 15 **2.3.2. *Ex situ* characterization**

35
36
37 16 XANES at the Ti K-edge were carried out after transferring the samples inside
38
39 17 SIRIUS High Vacuum (HV) diffractometer by means of a glove box.⁴² XANES spectra
40
41 18 were recorded by scanning the incoming energy step-by-step and measuring the
42
43 19 sample fluorescence with the four-element Silicon Drift Detector (SDD). The
44
45 20 beamline optics setup was the same as described above for the *in situ* XANES at the
46
47 21 Ti K-edge. For the Ti K-edge x-ray Linear Dichroism (XLD) spectra, selection of the
48
49 22 linear vertical polarization was obtained by changing the phase of the HU36
50
51 23 undulator: this allows us to change from linear vertical to linear horizontal
52
53
54
55
56
57
58
59
60

1
2
3 1 polarization without changing the sample position and preserving the grazing
4
5 2 incidence mode in all measurements.
6
7

8 3 Post-growth annealed samples have been characterized by Raman
9
10 4 Spectroscopy using a Renishaw In-Via spectrometer, equipped with a Peltier cooled
11
12 5 (CCD) detector. Raman spectra were recorded in the backscattering geometry. The
13
14 6 light was focused onto the sample surface by a 100 x (0.85 numerical aperture)
15
16 7 short working objective. The resulting spot diameter was around 0.7 μm . A 532 nm
17
18 8 laser diode was used as a light source with a typical laser power of 1 mW.
19
20

21 9 Transmission electron microscopy (TEM) observations were carried out at
22
23 10 200 kV with a Tecnai Osiris TEM (Thermo Fisher Scientific) and equipped with a high
24
25 11 brightness X-FEG gun and a Super-X Energy Dispersive x-ray (EDX) system
26
27 12 comprising four detectors.
28
29
30

31 13 Elemental chemical components and stoichiometry were examined by XPS
32
33 14 (x-ray Photoelectron Spectroscopy) and HAXPES (Hard x-ray Photoelectron
34
35 15 Spectroscopy) using a PHI *Quantes* with two different monochromatized sources,
36
37 16 either Al K_{α} ($h\nu=1486.6$ eV) or Chromium K_{α} ($h\nu = 5414.7$ eV). The use of the novel
38
39 17 lab-based hard x-ray sources (HAXPES) was required to investigate the oxidation of
40
41 18 the TiS_2 layer at the surface and the in-depth distribution, this was possible thanks
42
43 19 to the increase of the inelastic mean free path of electrons with increasing photon
44
45 20 energy (Chromium K_{α} , $h\nu = 5414.7$ eV)
46
47

48 21 Samples were prepared using a metallic clamp to ensure the electrical contact with
49
50 22 the sample holder. Measurements using Cr source have been done at fixed angle of
51
52 23 $\theta=45^\circ$ and for the Al one at different angles using Angle-Resolved XPS (or ARXPS)
53
54 24 ($\theta=15^\circ$, 45° , and 85°), where θ is the angle between the surface and the analyzer.
55
56
57

1
2
3 1 The thickness was calculated using the formula $d=3 \lambda \sin \theta$ where λ is the
4
5 2 photoelectron mean free path using TPP2M equation.⁴³ Data treatment of the
6
7 3 measured spectra were analyzed using CasaXPS software. For spectral calibration,
8
9 4 C 1s core peak from adventitious carbon was considered with binding energy at
10
11 5 284.8 eV.³⁸ A non-linear Shirley-type background was processed for peak fitting and
12
13 6 the deconvolution of the peaks was obtained using the weighted least-squares
14
15 7 calculation method of 30% Lorentzian and 70% Gaussian line shapes and Full Width
16
17 8 at Half Maximum (FWHM) constraints.³
18
19
20
21
22

23 **2.3.3 Four-point resistivity Measurements**

24
25 11 Four-point probe resistivity measurements were carried out at room temperature
26
27 12 using the Lucas-Signatone Labs Pro4 and a Keithley 2400 on 15 and 30 nm thick
28
29 13 TiS₂/100 nm-SiO₂ thin films synthesized from 40 and 80 ALD/MLD cycles and
30
31 14 annealing in Ar(96%)/H₂(4%) for 30 min at 450°C. Five acquisitions were performed
32
33 15 on different spots of the film surface and substrate to check the homogeneity and
34
35 16 calculate an average of the resistivity. The mean resistivity was obtained by
36
37 17 multiplying the sheet resistance value ($\Omega.\text{sq}^{-1}$) by the thickness of the deposited
38
39 18 layer. The resistivity value of the bare 100 nm-SiO₂ on silicon was too high to be
40
41 19 measured with the equipment.⁴⁴
42
43
44
45
46
47

48 **2.3.4. Spectroscopic Ellipsometry**

49
50 22 Spectroscopic ellipsometry (SE)⁴⁵ measurements were performed using two
51
52 23 Woollam ellipsometers (RC2 in the 210-2500 nm wavelength range and IR-VASE in
53
54 24 the mid-infrared range). The complex refractive indexes of 15 and 30 nm thick
55
56
57
58
59
60

1
2
3 1 TiS₂/100 nm-SiO₂ thin films obtained from 80 ALD/MLD cycles and annealed in
4
5 2 Ar(96%)/H₂(4%) for 30 min, was derived from the ellipsometric measurement using
6
7 3 a sum of 9 Gaussian oscillators. The complex refractive index was described as $N =$
8
9 4 $n + ik$, where n and k are the real and imaginary part of N . The imaginary part is
10
11 5 related to the absorption coefficient α by the formula $\alpha = 4\pi k/\lambda$, where λ is the
12
13 6 wavelength. The bandgap of the samples were calculated using the Tauc-Plot⁴⁶
14
15 7 which is a representation of the function $(\alpha h\nu)^n$ versus the photon energy ($h\nu$,
16
17 8 where h is the Planck constant).
18
19
20
21 9
22
23
24
25
26
27
28
29
30
31
32
33
34
35
36
37
38
39
40
41
42
43
44
45
46
47
48
49
50
51
52
53
54
55
56
57
58
59
60

3. Results

3.1. Molecular study of ALD/MLD process on silica beads substrate

3.1.1 *Chemical reactions between the two molecular precursors in absence of substrate*

Exposure of TDMAT to EDT leads to the immediate formation of an orange precipitate in pentane, while each molecule separately is soluble in pentane at the given concentrations with no formation of solid. The formation of the orange precipitate shows the existence of a thermodynamically favorable and kinetically facile pathway reaction between the two precursors. The analysis of the orange precipitate by solid-state ^{13}C NMR (see **Fig. S1**) displayed resonances compatible with the presence of organic moieties originating from EDT residues. The solid displays a weak Electron Paramagnetic Resonance (EPR) signal at $g=1.98$ (see **Fig. S2**), assigned to titanium(III) centers.⁴⁷

3.1.2 *Successive reactions at the gas-solid interphase between the two molecular precursors and silica beads surface*

Further insight in the ALD/MLD steps of the process was obtained by reacting the precursors with silica beads, a pertinent model for studying the reaction occurring at the gas /solid interphase between precursors and substrates such as silicon-covered wafers.²⁵ The modeling hereafter describes the evolution during the second ALD/MLD cycle as well as during the sixth ALD/MLD cycle to show the repeatability of the surface chemistry (see **Scheme 1**).

3.1.2.1. *Metal pulses on silica beads.*

1
2
3
4 1 The *in situ* infrared (IR) spectra of solids **1**, **2**, and **3** (that is at the beginning,
5
6 2 during, and at the end of the second ALD/MLD cycle, see **scheme 1**) are presented
7
8 3 in **Figure 2**. The most relevant feature of the IR spectrum of sample **1** in the context
9
10 4 of the ALD/MLD mechanism studied here is the presence of a band at 2412 cm^{-1}
11
12 5 assigned to $\nu(\text{S-H})$. The broad band between 2600 and 3200 cm^{-1} is assigned to
13
14 6 hydrogen-bonded thiol moieties. Signals around $2700\text{-}3000\text{ cm}^{-1}$ correspond to C-H
15
16 7 stretching vibrations arising from organic ligands. After the metal pulse, the
17
18 8 spectrum of the resulting solid **2** showed an increase of the IR absorption band
19
20 9 between 2700 and 3000 cm^{-1} (see blue Diffuse Reflectance Infrared Fourier
21
22 10 Transform (DRIFT) spectrum, curve 2 in **Figure 2**), together with the reduction of
23
24 11 the broad S-H stretching signals. Similar though shallower changes can be observed
25
26 12 in spectra of **9** and **10** (see SI **Fig. S3**). Indeed, the analytic changes from one early
27
28 13 cycle to the next are expected to be sharper than from a later cycle to the next,
29
30 14 even if the surface chemistry remains similar, given the larger relative change that
31
32 15 one single pulse is expected to bring to an early deposit than to a later one.
33
34 16 Furthermore, in agreement with the other analytic data presented below, and as
35
36 17 lengthily discussed in the next section (see § 4.1.3), the metal coverage is less
37
38 18 efficient in the later cycles, leaving more unreacted thiols after the metal pulse thus
39
40 19 explaining the large feature at 2412 cm^{-1} assigned to S-H, in spectrum **10** (**Fig. S3**)
41
42 20 with respect to its almost complete absence in spectrum **2** (**Figure 2**).
43
44
45
46
47
48
49
50
51
52
53
54
55
56
57
58
59
60

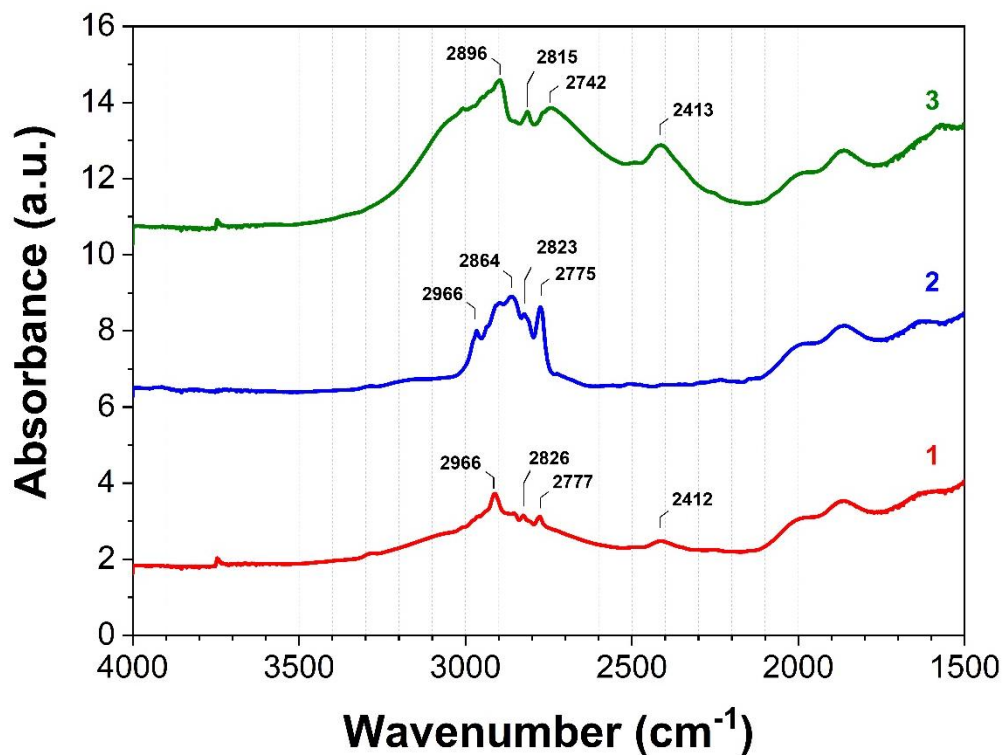


Figure 2: IR absorbance spectra recorded during the second ALD/MLD cycle on silica nanobeads SiO₂₋₇₀₀ (spectrum of **1**, red); after the ALD pulse of TDMAT (spectrum **2**, blue); after the subsequent MLD pulse of EDT (spectrum **3**, green), see **Scheme 1** for numbering.

The chemical composition of solids was determined by elemental analysis (see **Table 1**). The elemental analyses of the solids resulting from the metal pulses of the 2nd and 6th ALD/MLD cycles, *i.e.* **2** and **10**, show substantial increase in the metal content, indicating a successful metal grafting in both cases.

Table 1: Results of elemental analyses (expressed in weight percent, %_{wt}) of the solids obtained during the 2nd and 6th ALD/MLD cycles using TDMAT and EDT alternating pulse on SiO₂₋₇₀₀ nanobeads. See **Scheme 1** for numbering scheme.

	Elemental analysis (wt%)					Atomic ratios		
	Ti	C	N	S	H	C/Ti	N/Ti	S/Ti
1	1.7	2.2	0.9	2.6	0.5	5.3	1.9	2.3
2	3.0	3.9	1.8	2.8	0.9	5.3	2.0	1.4
3	2.8	5.15	1.3	7.7	1.1	7.2	1.5	4.1
...								
9	4.9	9.8	2.2	15.8	2.2	8.0	1.5	4.8
10	5.5	10.3	2.4	16.1	2.3	7.4	1.5	4.3
11	5.3	10.8	2.3	17.8	2.4	8.1	1.5	5.0

During the 2nd metal pulse, the volatiles released upon TDMAT addition to **1** were collected and analysed. Dimethyl amine was observed as the sole volatile by-product of the reaction (see ¹H NMR study of the condensed volatile by-products in **Fig. S4**), corroborating the successful reaction of the amido precursor TDMAT at the gas-solid interphase of the growing thiolate layer.

3.1.2.2. EDT pulses on silica beads.

The sulphur pulse has been modelled by analysing the addition of EDT to the metal-terminated silica beads, **2** and **10**, followed by a purging step, leading to solids **3** and **11**, that is during the second halves of the second and sixth cycle, respectively (see **Scheme 1**).

1
2
3 1 The DRIFT spectrum for **3** (**Figure 2**, green line) exhibits a characteristic S–H
4 bond stretching (2413 cm^{-1}) which had all but disappeared in the spectrum of **2**
5 (**Figure 2**, blue line) and broadening of the bands between 2700 and 3000 cm^{-1} ,
6
7
8
9
10
11
12
13
14
15
16
17
18
19
20
21
22
23
24
25
26
27
28
29
30
31
32
33
34
35
36
37
38
39
40
41
42
43
44
45
46
47
48
49
50
51
52
53
54
55
56
57
58
59
60

1
2
3
4
5
6
7
8
9
10
11
12
13
14
15
16
17
18
19
20
21
22
23
24
25
26
27
28
29
30
31
32
33
34
35
36
37
38
39
40
41
42
43
44
45
46
47
48
49
50
51
52
53
54
55
56
57
58
59
60

The DRIFT spectrum for **3** (**Figure 2**, green line) exhibits a characteristic S–H bond stretching (2413 cm^{-1}) which had all but disappeared in the spectrum of **2** (**Figure 2**, blue line) and broadening of the bands between 2700 and 3000 cm^{-1} , which indicates a successful chemisorption of the thiol. ^1H NMR analysis of the trapped volatile by-products displayed a typical resonance corresponding to methyl protons of HNMe_2 (see **Fig. S5**). The changes in elemental analysis are reported in **Table 1**. The sulphur-containing solids are also EPR active (see **Fig. S2**).

3.2. ALD/MLD growth followed by annealing crystallization process on silica-terminated silicon wafers and monitoring with operando x-ray studies

11 The ALD/MLD growth process is based on alternating additions of TDMAT and EDT
12 pulses to the wafer, followed by a subsequent thermal annealing of the ALD/MLD
13 grown layer inside a dedicated reactor. This reactor, permits to control a full
14 understanding of the atomistic mechanisms during process, as it was observed by
15 previous work done in our research group.^{40,48–52}

3.2.1 ALD/MLD growth by alternate TDMAT and EDT pulses

3.2.1.1. In situ monitoring of titanium thiolate MLD growth by MWE and XRR

19 **Figure 3(a)** shows thickness evolution during 40 growth cycles recorded by *in*
20 *situ* ellipsometry and fitted using a $\text{TiO}_2/100\text{ nm-SiO}_2/\text{Si}$ thin film model⁴¹. Though
21 such a crude model prevents a quantitative analysis of the data, the thin film final
22 thickness value measured by *in situ* XRR (13.3 nm) is compatible with the one
23 estimated by MWE (18.2 nm). Besides, the ellipsometry data allow to ensure that

1 the process is robust and reproducible under SOLEIL x-ray experimental conditions.
2 The periodic changes and saturation of the signal during the purge testify to self-
3 limiting alternating surface reactions that insures an ALD/MLD process, as
4 highlighted by the inset of **Figure 3(a)** showing the as-calculated total film thickness
5 increase during a single full cycle.

6 Monitoring the reflected x-ray intensity provides more quantitative insights
7 on the growth. Provided that the film roughness is not too high, the specular
8 reflected beam intensity recorded during the deposition, at a fixed incident angle,
9 oscillates as a function of cycle number (time) due to the film thickness evolution.
10 A maximum (resp. minimum) of intensity corresponds to constructive (resp.
11 destructive) interference of the beams reflected at the growing film surface and at
12 the film/SiO₂ interface. Then, knowing the thickness oscillation period in the steady
13 growth regime, it is possible to relate the increase of intensity inside one half an
14 oscillation period to the film thickness increase. **Figure 3(b)** shows the increase in
15 film thickness with the number of cycles in the range [11-17].

16 3.2.1.2. *In situ* monitoring of titanium thiolate ALD/MLD growth by XRF

17 Element-specific *in situ* analyses during the growth were obtained by
18 monitoring Ti and S X-ray Fluorescence (XRF) during each successive ALD and MLD
19 step, respectively, to quantify the Ti and S amount deposited on the sample surface.
20 **Figure 3 (c,d)** shows Ti and S K_α fluorescence intensities normalized to the incoming
21 x-ray beam intensity, respectively, as a function of ALD/MLD cycle number. The
22 filled circles correspond to the fluorescence mean intensity at the end of each cycle
23 (that is after the EDT purge). Overall, each fluorescence appears to increase linearly

1
2
3 1 after a short transient regime of growth (see linear regression fits calculated over
4
5 2 the last 15 cycles, in the steady linear regime of growth).
6
7

8 3 The inset of **Figure 3(c)** and **Figure 3(d)** show the XRF intensity variation
9
10 4 during the 30th to 34th cycle, representative of cycles in the steady state regime of
11
12 5 growth, giving an insight in chemical reactions occurring at the gas-solid interphase
13
14 6 during each pulse in the steady state. In both cases, an overall fluorescence increase
15
16 7 is observed suggesting a successful grafting at each pulses. Some differences are
17
18 8 also visible between the TDMAT and the EDT pulse. As for the Ti fluorescence, an
19
20 9 initial decrease of intensity during the injection of TDMAT is observed. This drop in
21
22 10 intensity is assigned to the presence of the TDMAT carrier gas (Ar), which leads to
23
24 11 a significant absorption of the Ti K α XRF because the Ti K α energy (4509 eV) is a bit
25
26 12 larger than the Ar K edge (3206 keV) ; upon removal of argon through the nitrogen
27
28 13 purge the effective increase in titanium fluorescence is observed, confirming
29
30 14 titanium enrichment of the ALD growing phase. No change in Ti fluorescence is
31
32 15 observed after the EDT pulse, as expected since no change in titanium content is
33
34 16 expected in the second half pulse of each cycle. As for the S fluorescence, the
35
36 17 aforementioned drop in intensity due to the presence of argon is also observed
37
38 18 during the TDMAT pulse but the net effect after the nitrogen pulse is null on the S
39
40 19 fluorescence as expected. In this case, the net fluorescence increase is observed
41
42 20 only after the EDT half-cycle. Noteworthy, the spikes of XRF intensities at the S edge,
43
44 21 notably at low cycle number, evidence the desorption of S-containing molecules,
45
46 22 including EDT, from the surface, suggesting that physisorbed and chemisorbed EDT
47
48 23 are present after the EDT purge and the physisorbed excess EDT (and possibly other
49
50 24 gaseous by-products), can be correctly removed by the nitrogen purge step. To sum
51
52
53
54
55
56
57
58
59
60

up, the XRF data shown in **Figure 3 (c,d)**, also evidence a well-behaved self-limiting alternating deposition by ALD/MLD of a titanium-containing thiolate layer.

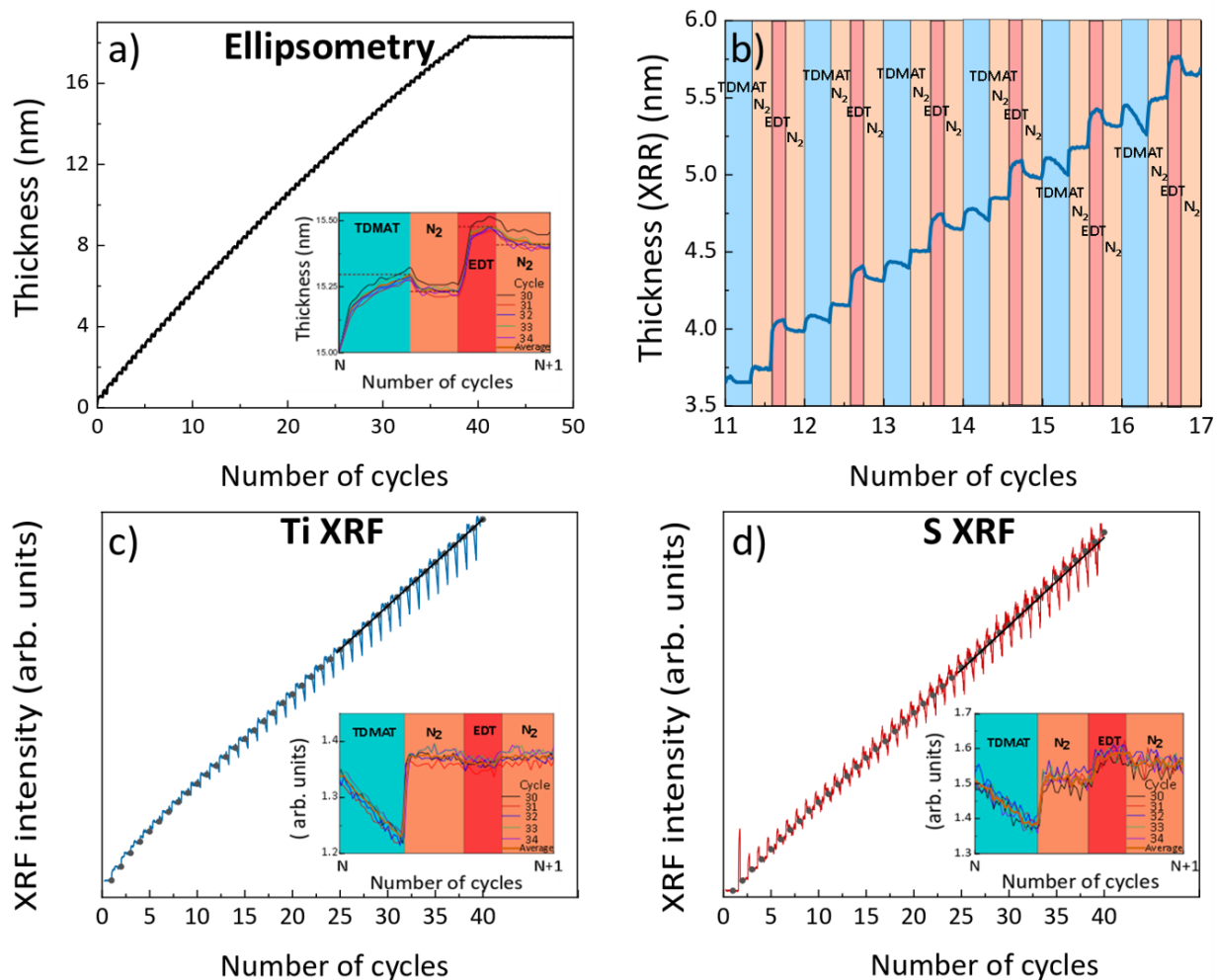


Figure 3: Film thickness evolution measured by (a) multiwavelength ellipsometry (b) XRR at fixed angle. Ti K_{α} XRF intensity (blue line, c) and S K_{α} XRF intensity (red line, d); in both cases, the mean intensity value at the end of the EDT purge is shown for each cycle (closed black circles) together with the regression line calculated in the linear steady state regime of growth (black lines, $R^2=0.998$ and 0.992 , respectively). All data were recorded in situ as function of the number of cycles during the Ti-thiolate deposition ($T_{\text{substrate}} = 50\text{ }^{\circ}\text{C}$). The insets in (a), (c) and (d) show the raw data obtained during cycle numbers 30, 31, 32, 33 and 34, the curves were rescaled to be superposed.

1
2
3 1 *3.2.1.3. X-ray Absorption Near Edge Structure (XANES) of Ti-thiolate sample*
4
5 2 *grown by ALD/MLD*
6
7

8 3 The XANES spectra recorded at the Ti K-edge of the as-deposited Ti-thiolate
9
10 4 thin film is reported in **Figure 4(a)**. The incoming x-ray beam linear polarization was
11
12 5 set parallel to the growth surface. Its pre-edge peak position is at slightly lower in
13
14 6 energy ($\Delta E=1$ eV), with respect to the pre-edge peak position of the XANES spectra
15
16 7 of the annealed samples (**Figure 4 (b,c,d)**); these overlap with the pre-edge peak
17
18 8 position in the XANES spectrum of the reference TiS_2 powder, **Figure 4(e)**. The latter
19
20 9 is a spectrum averaged over the beam polarization orientation with respect to the
21
22 10 hexagonal crystallographic frame of the lamellar 1T-TiS_2 structure because the
23
24 11 sample is a powder. The higher energy pre-edge peak, observed in the energy range
25
26 12 [4972-4973] eV (A1 feature in **Figure 4**), is well understood with regard to the 1T-
27
28 13 TiS_2 structure.⁵³. While the detailed analyses of the XANES data are beyond the
29
30 14 scope of this paper, the energy difference between the feature of the as deposited
31
32 15 thiolate sample (**Figure 4a**) and the one of TiS_2 (**Figure 4e**) corroborates the
33
34 16 presence of the Ti(III) centers in the as-deposited material, as anticipated by the
35
36 17 modeling studies reported above.
37
38
39
40
41
42
43
44
45
46
47
48
49
50
51
52
53
54
55
56
57
58
59
60

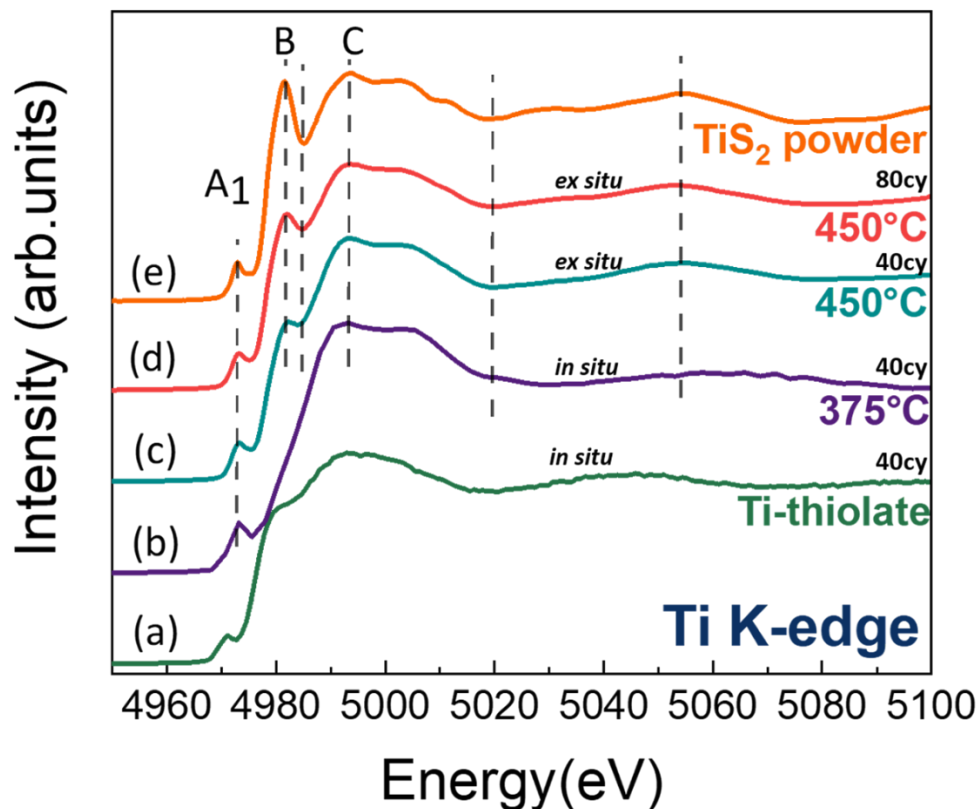


Figure 4: In situ XANES spectra at the Ti K-edge of (a) as-deposited Ti-thiolate sample obtained after 40 cycles of ALD/MLD growth and (b) after annealing under $H_2(4\%)/Ar(96\%)$ gas at $375^\circ C$ for 30 minutes. Ex situ XANES spectra of Ti-thiolate samples, obtained after (c) 40 cycles and (d) 80 cycles of ALD/MLD growth and annealing at $450^\circ C$ for 30 minutes; (e) ex situ XANES spectrum of a reference TiS_2 powder recorded in fluorescence mode. The linear polarization of the x-ray beam was parallel to the growth surface.

3.2.2 Characterization of TiS_2 nano domains obtained by annealing the Ti-thiolate grown by ALD/MLD

Two Ti-thiolate samples obtained by 40 and 80 ALD/MLD cycles, respectively, were annealed at $450^\circ C$ for 30 min under $H_2(4\%)/Ar(96\%)$ gas, H_2 being known to facilitate sulphur extrusion from sulphur-rich TiS_{2+x} phases.⁵⁴ The resulting phases were examined by XANES, Raman scattering spectroscopy, TEM, X-ray absorption

1
2
3 1 linear dichroism, and HAXPES to study their composition, crystallinity, and
4
5 2 microstructure.
6
7 3
8
9

10 4 3.2.2.1 X-ray Absorption Near Edge Structure (XANES) of the TiS_2 samples 11 12 5 *obtained by annealing* 13

14 6 The XANES spectra of the two annealed samples are reported in **Figure 4(c**
15
16 7 **and d**, respectively). In all cases, the pre-edge peak in the energy range [4972-4973]
17
18 8 eV (see A1 in **Figure 4**), well understood with regard to the 1T- TiS_2 structure⁵³, is
19
20 9 observed. Ti^{4+} atoms in 1T- TiS_2 structure (electronic configuration: $3d^04s^0$) sit on a
21
22 10 1a position (point group $-3m$) of the $\text{P}\bar{3}m1$ space group. The crystal has no inversion
23
24 11 symmetry about this position, allowing the local hybridization of the central Ti 4p
25
26 12 states with near neighbor Ti 3d orbitals.⁵³ Since Ti first nearest neighbors comprise
27
28 13 six sulphur atoms which form a centrosymmetric octahedron, the A1 feature
29
30 14 intensity is ascribed mainly to the dipole transition from Ti 1s to 4p character of the
31
32 15 3d band. Peaks B and C arise from transitions to final Ti 4p states.
33
34
35

36 16 Noteworthy, the pre-edge peak energy positions for all annealed samples
37
38 17 and TiS_2 powder are the same, indicating the same formal valence of the central Ti
39
40 18 atom (Ti^{4+}), unlike the slightly lower energy (1 eV) shifted pre-edge peak position of
41
42 19 the sample before annealing (see **Figure 4(a)**), indicating the full conversion of the
43
44 20 Ti(III) centers present in the as-deposited material to the expected Ti(IV) state
45
46 21 present in TiS_2 . As shown by comparing **Figure 4(c,d)**, the 80-cycles sample displays
47
48 22 significantly improved atomic local order after annealing, with respect to the 40-
49
50 23 cycle sample after annealing, with the local density of states tending to the one of
51
52 24 TiS_2 . Such a result could indicate that the range of atomic local order and texture
53
54 25 reached during the annealing improve upon film thickness and the relative amount
55
56
57
58
59
60

1 of Ti atoms in oxidized regions at the sample surface and sulfide/SiO₂ interface is
2 smaller in the case of the 80-cycles thin film (in agreement with TEM evidence
3 below).

4 XANES spectra was also recorded *in situ* during the annealing of the sample
5 obtained after 40 MLD cycles. **Figure 4(b)** shows the Ti K-edge XANES spectra after
6 annealing at 375 °C for 30 min under H₂(4%)/Ar(96%) gas. The quantitative analysis
7 of the spectra before and after annealing (**Figure 4(a)** and **(b)**, respectively) is out
8 of the scope of this article. After annealing at 375 °C the spectrum shows some
9 substantial similarities to the TiS₂ powder spectrum, firstly the increase of the
10 distinctive pre-edge features of TiS₂. At the same time, it is clear that the TiS₂ atomic
11 arrangement is not yet achieved and is much poorer than the one observed by
12 annealing at 450 °C (see **Figure 4(c,d)**). Therefore, the annealing temperature
13 increase to 450 °C seem to significantly improve the atomic local order which tends
14 to the one of TiS₂, as the TEM results shown hereafter will also show.

16 3.2.2.2 Raman scattering spectroscopy

17 Among the fundamental active modes in Raman spectroscopy, two modes
18 are associated to 1T-TiS₂ (space group P $\bar{3}$ m1): the E_g mode (≈ 234 cm⁻¹) and A_{1g}
19 mode (≈ 336 cm⁻¹), corresponding to vibrations of the sulphur atoms in and out of
20 the S-Ti-S layer, respectively. An additional shoulder mode (termed Sh-shoulder or
21 Sh herein, ≈ 372 cm⁻¹) appears more pronounced for S-Ti-S multilayer than
22 monolayer structure.^{32,55-60} The appearance of the Sh-shoulder mode is due to an
23 excess of metal atoms between the TiS₂ layers (in the van der Waals gaps) resulting
24 in local stiffness of the phonons.³²

1
2
3 1 The Raman scattering spectra of the two annealed samples obtained after 40
4
5 2 and 80 cycles, respectively, were measured with an excitation frequency in the
6
7 3 visible range (532 nm), **Figure 5(a,b)**. The two spectra display the Eg and A1g active
8
9 4 modes corresponding to 1T-TiS₂. The shoulder mode (Sh) is visible at about 380 cm⁻¹.
10
11 5 ¹. By comparison with the results found in the literature and obtained with a
12
13 6 reference TiS₂ powder, the spectra indicate a good crystalline quality of the samples
14
15 7 with likely some defects in between the layers as corroborated by the presence of
16
17 8 the Sh mode.^{32,38}

19
20 9 The frequency difference between A1g and Eg modes is correlated to the
21
22 10 average number of stacked TiS₂ layers. However, the determination of the
23
24 11 frequency difference with precision remains difficult due to a significant
25
26 12 asymmetry³² of the Eg mode intensity profile (see **Figure 5(a,b)**). For this reason,
27
28 13 the A1g mode and the better-defined Sh-shoulder mode should be preferred for
29
30 14 the determination of the number of layers. Indeed, it has been observed in the
31
32 15 literature that the shoulder mode (Sh) appears being more pronounced for
33
34 16 multilayers than for a monolayer. The ratio of the integrated intensity profiles of
35
36 17 the A1g and Sh-shoulder (A1g/Sh) can then be used for the determination of the
37
38 18 number of TiS₂ layers (up to 5).^{32,55} The obtained values show the presence of
39
40 19 multilayers with more than 5 layers for both samples, in line with TEM images (see
41
42 20 **Figure 5(c,d)**). By normalizing the spectra of both samples to the T2g Si peak, the
43
44 21 integrated intensity of the A1g peak of the 40-cycle sample is half of the one of the
45
46 22 80-cycle sample, in agreement with the film thickness ratio (see **Fig. S6**).
47
48
49
50
51
52
53
54
55
56
57
58
59
60

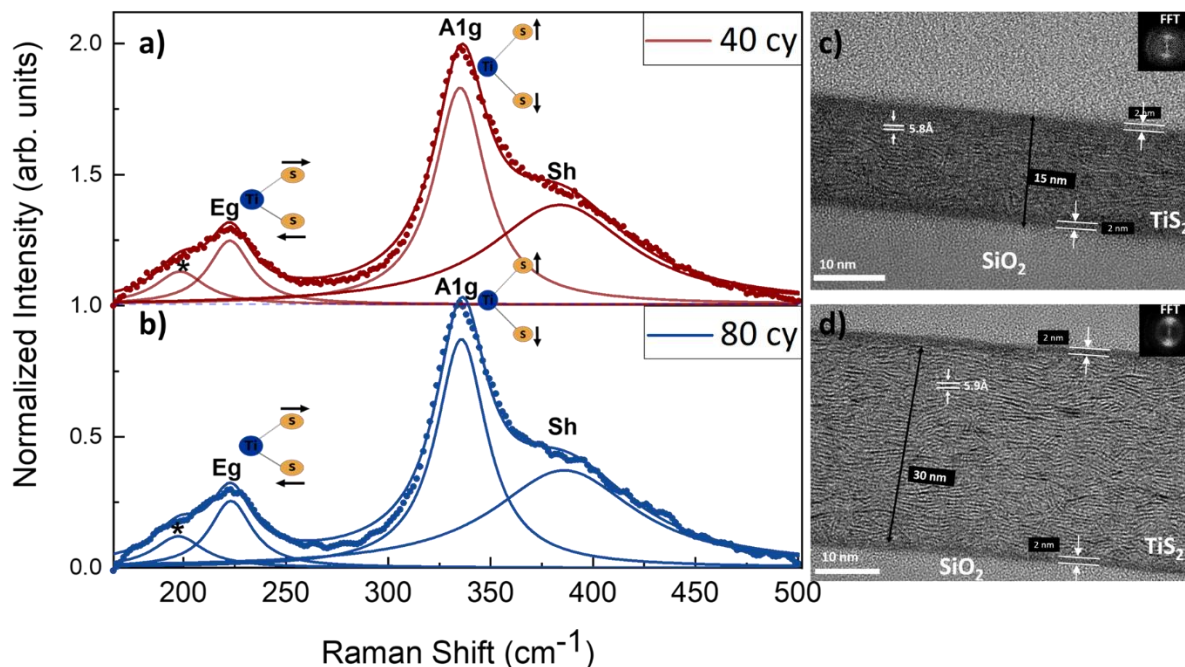


Figure 5: (a, b) Raman spectra (dotted lines) and (c, d) cross-section TEM images of samples resulting from (a, c) 40 and (b, d) 80 ALD/MLD cycles and an annealing at 450 °C for 30 min under H₂(4%)/Ar(96%) gas. The insets in the TEM images represent the fast Fourier transform of the sample image. Raman spectra were normalized to the intensity of the A1g mode and fitted with Lorentzian curves (solid lines in a) and b) panels).

3.2.2.3 Electron microscopy.

TEM images of the two annealed samples reveal continuous thin films with low surface roughness (see **Figure 5 (c,d)**). The nanoscale structure of the bulk of the grown phase (that is not taking into account the 2 nm thick ultimate surface and the 2 nm thick interlayer surface with the wafer substrate, both discussed below) confirms the presence of partly ordered crystalline nanodomains of atomically thin stacks of TiS₂ layers, in agreement with the Raman data discussed above. The interlayer distances equal to 5.8±0.2 Å for the 40-cycles and 5.9±0.2 Å for the 80-cycles samples are close to the bulk 1T-TiS₂ c-parameter, 5.7 Å⁶¹. According to the TEM images, the thickness of the deposit is, as expected, almost double for the 80-

1
2
3 1 cycles than for the 40-cycles sample (30 nm and 15 nm, respectively). The TEM
4
5 2 images reported in **Figure 5 (c,d)** show some more pronounced atomic short-range
6
7 3 order in the thicker 80 cycle sample than in the 40 cycle one. Regarding the ultimate
8
9 4 surface, for both samples, the sulfide thin film is covered by an amorphous ca. 2
10
11 5 nm-thick top layer, which presumably results from the hydrolysis and oxidation of
12
13 6 the material exposed to air, and should therefore be titanium oxysulfide. At the
14
15 7 bottom, the sulfide layer/SiO₂ interface stays rather sharp. The narrowness (ca. 2
16
17 8 nm thick) of such interface layer, which is expected to be an oxysulfide resulting
18
19 9 from the first pulses of the metal precursor with the pristine ultimate surface of the
20
21 10 siliceous substrate²⁵, suggests a well-defined seeding chemistry from the very first
22
23 11 pulses of the process.
24
25
26
27
28
29

30 13 *3.2.2.4 Hard x-ray Photoelectron Spectroscopy (HAXPES) of annealed samples*

31
32 14 In order to perform in-depth study of both the stoichiometry and chemical
33
34 15 elemental components of the 30 nm thick TiS₂ thin film obtained with 80 ALD/MLD
35
36 16 cycles and annealed at 450 °C, HAXPES was carried out using chromium K_α x-ray
37
38 17 sources.
39
40

41
42 18 The analytical information depth using Cr K_α source ($h\nu = 5414.7$ eV) is about
43
44 19 three times deeper than with the Al K_α source. The benefit of a larger sampling
45
46 20 depth opens opportunities to minimize the contribution of the upper surface of the
47
48 21 sample, possibly altered by the atmosphere, in the overall spectra, TiS₂ being known
49
50 22 to convert to TiO_x by exposure to air.⁶² The presence of adventitious air oxidation
51
52 23 and hydrolysis of the top thin film (see **Figure 5(d)**), is demonstrated in a qualitative
53
54 24 way by comparing the **Ti 1s** core level spectra to the **Ti-2p** core level spectra
55
56
57
58
59
60

presented in **Figure 6**. The mean free path of the photoelectrons calculated using TPP2M equation,⁴³ is found to be larger for the Ti 2p (8.1 nm) than that of the Ti 1s (1.6 nm). It follows that the analyzed thickness is about 3.3 nm with the Ti-1s core level peak instead of 15.7 nm with the Ti-2p and S-2p peaks.

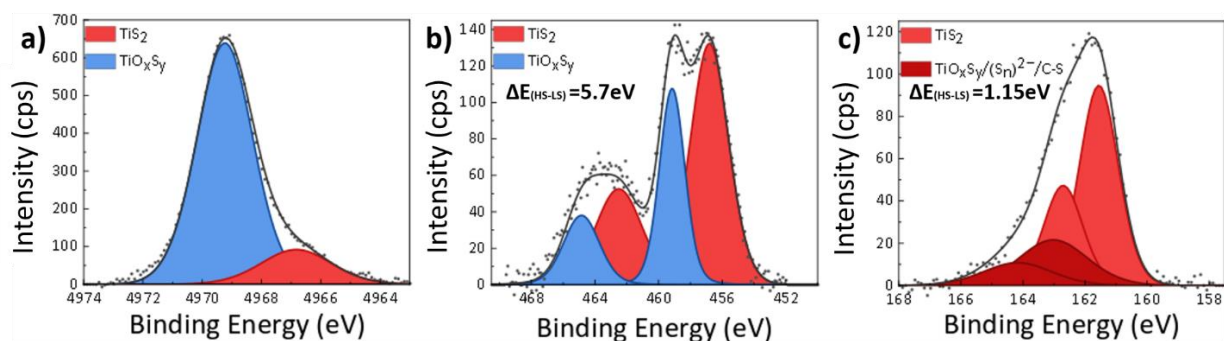


Figure 6: HAXPES spectra measured with the Cr $K\alpha$ source: Intensity as a function of the electron binding energy a) Ti-1s core peaks b) Ti-2p core peaks (doublets) and (c) S-2p core peaks (doublets).

The Ti-1s XPS spectra shown in **Figure 6(a)** present two different environments: the strong signal at 4969.3 eV (84.7%, blue peak) is attributed to titanium oxysulfides whereas the weak one at 4966.8 eV (15.3 %, red peak) is attributed to TiS_2 layers. For the signal at 4969.3 eV, the thickness of the oxide layer on the top of the deposited TiS_2 layer is about 2.1 nm. The latter is in agreement with the value found by ARXPS with an Al source (see **Fig. S7**).⁶³ Interestingly, the oxidation of the top layer of the sample was also checked by monoatomic Ar ions etching and in-depth oxygen profiling, attesting to the absence of oxygen contamination inside the thin film (see oxygen profile **Fig. S8** in SI).

The Ti 2p XPS spectra shown in **Figure 6(b)** present two different Ti $2p_{3/2}:2p_{1/2}$ spin-orbit doublets. The most intense (456.8 eV and 462.5 eV) corresponds to TiS_2 .^{55,64,65} The other one (459.2 eV and 464.9 eV) is assigned to the oxysulfide layer present on the top of the obtained TiS_2 .^{64–67} The S-2p XPS spectrum shown in **Figure**

1
2
3 1 **6(c)** presents also two S $2p_{3/2}$: $2p_{1/2}$ components. The intense doublet (161.6 eV and
4
5 2 162.7 eV, spin-orbit doublet of S^{2-} species) corresponds to TiS_2 .^{64,67} The weak
6
7 3 doublet signal (163.0 eV and 164.2 eV) could be attributed to the spin-orbit doublet
8
9 4 of $(S_n)^{2-}$ species (where $n=2,4,6..$) known as an S-S pair and to C-S bonds. Based on
10
11 5 the widening of the peak component presented in **Figure 6(c)** we attribute this
12
13 6 component to a combination of $(S_2)^{2-}$ and $(S_4)^{2-}$ species.⁶⁸ It can also be referred to
14
15 7 titanium oxysulfide environment in connection with the oxidized part already
16
17 8 detected on the surface of the TiS_2 layer.^{38,66,69,70}

9
10 Theoretical Relative Sensitivity Factors (RSF) were used to quantify the
11
12 stoichiometry of the obtained TiS_2 layers.⁷¹ The calculated aspect ratio $[S]/[Ti]$
13
14 calculated with the Ti2p and S2p doublets attributed to TiS_2 is equal to 2.1. This
15
16 indicates that the deposited film has a stoichiometry close to the one expected for
17
18 TiS_2 . To correlate and compare the results of HAXPES obtained with the Cr source,
19
20 XPS spectra were measured with the conventional monochromatic soft Al source
21
22 (Aluminum K_{α} , $h\nu = 1486.6$ eV) at three different angles ($\theta=15^\circ, 45^\circ$ and 85° with
23
24 respect to the sample surface normal) for which the depth of analysis are equal to
25
26 2.3, 4.9 and 6.8 nm, respectively. The results are listed in supporting Information
27
28 (see **Fig. S7**), the aspect ratio $[S]/[Ti]=1.9$ is in agreement with the stoichiometry
29
30 obtained with the Cr source. **Table S1** shows the chemical composition proposed
31
32 based on the XPS measure at the Al source and overall suggest the presence of the
33
34 same environments for Ti-2p and S-2p core peaks for both the Al and Cr sources.
35
36
37
38
39
40
41
42
43
44
45
46
47
48

49
50 ARXPS data shows large amount of carbon (21%) inside the obtained layer
51
52 (see **fig. S7 (i)**) which is not significantly affected by the change in take-off angle.
53
54 The C 1s core level spectra exhibit three components originating from different
55
56 sources. The major part corresponds to C-H/C-C bonding, it could originate from
57
58
59
60

1
2
3 1 adventitious carbon but also from the incomplete reaction of TDMAT³⁵ or the
4
5 2 presence of graphitic carbon, as it was shown in a previous study regarding the
6
7 3 synthesis of MoS₂ by the same MLD/ALD-annealing approach.²⁵ The presence of
8
9 4 oxidized carbons (C-O and C=O, attributed to the as weaker contributions at 286.6
10
11 5 and 289.1 eV respectively, could originate from the surface contamination due to
12
13 6 the exposure to ambient conditions³⁸. Note that the line at 286.6 eV could also be
14
15 7 assigned to C-S bonds indicating an incomplete reaction of EDT (HSCH₂CH₂SH).
16
17
18
19 8

9 3.2.2.5 x-ray absorption linear dichroism

10 The x-ray absorption linear dichroism at the Ti K-edge. **Fig. S9** in Supporting
11 Information shows polarized Ti K-edge XANES spectra recorded with the incoming
12 x-ray beam polarization parallel or perpendicular to the sample surface. The
13 polarization effect in the XANES spectrum confirms the anisotropic nature of the
14 obtained films. This was confirm at a larger scale that the e TEM images that the
15 TiS₂ monolayers are not randomly oriented, but tend to be parallel to the substrate
16 surface, *i.e.* the thin films show a partial texture.
17
18
19

20 3.2.2.6 Four-point probe electrical measurements and bandgap properties

21
22
23
24
25
26
27
28
29
30
31
32
33
34
35
36
37
38
39
40
41
42
43
44
45
46 20 Four-point probe resistivity measurements were carried out at room
47
48 21 temperature on the 15 nm and 30 nm thick TiS₂ thin film synthesized from 40 and
49
50 22 80 ALD/MLD cycles and annealed in Ar(96%)/H₂(4%) for 30 min at 450°C.

51
52
53 23 The mean resistivity equal to 6.61(0.4)x10⁻³ Ω.cm and 8.60(0.9)x10⁻³ Ω.cm for
54
55 24 the 15 and 30 nm thick films, respectively. The small dispersion in the values from
56
57
58
59
60

1
2
3 1 one spot to another attests to the homogeneity of the deposited samples. Such low
4
5 2 mean resistivity value is in the range of values for a semi-conductor materials at
6
7 3 room temperature. Regardless of some carbon amount in the TiS₂ thin film, a semi-
8
9 4 conductor material has been obtained. Recently, Basuvalingam *et al.*³⁸ reported the
10
11 5 growth of TiS₂ and TiS₃ layers using both thermal ALD and Plasma Enhanced-ALD
12
13 6 from TDMAT and H₂S: Ar. Thermal ALD sample grown at 100°C lead to TiS₂ thin films
14
15 7 with a resistivity equal to 2x10⁻³ Ω.cm ; PE-ALD samples grown at 150°C and 200°C
16
17 8 lead to TiS₂ thin film with resistivity values decreasing from 9x10⁻³ to 3.5x10⁻³ Ω.cm.
18
19 9 We can therefore conclude that our ALD/MLD process for the growth of TiS₂ thin
20
21 10 films allows us to synthesize a material whose resistivity is in the same order of
22
23 11 magnitude was obtained comparing to thermal ALD and PE-ALD process. Such a
24
25 12 result could lead to use TiS₂ films as 2D contact materials with 2D semiconductors
26
27 13 in device fabrication.
28
29
30

31
32 14 Semiconductor bandgap properties of the two samples with different
33
34 15 thicknesses (15 and 30 nm) were investigated by spectroscopic ellipsometry (SE)⁴⁵.
35
36 16 **Fig. 7** shows the experimental function $(\alpha hv)^2$ versus hv . The n and k curves as a
37
38 17 function of photon energy are shown in inset of **Fig. 7**. The onset of the absorption
39
40 18 above 1 eV indicates the existence of an optical bandgap. The linear relationship
41
42 19 between $(\alpha hv)^2$ and the energy at the absorption onset, is indicative of the
43
44 20 existence of a direct band gap. By extrapolating the linear regime down to the cross
45
46 21 point with the abscissa axis, a bandgap energy equal to 1.72 eV for the annealed
47
48 22 sample obtained by 80 ALD/MLD cycles, a value which is very close to the one
49
50 23 obtained with the 40 ALD/MLD cycles sample ($E_g=1.74$ eV). Noteworthy, a direct
51
52 24 band gap equal to 1.70 eV was found in crystalline one-dimensional hybrid
53
54 25 organic/inorganic TiS₂ (ethylenediamine) framework.⁷²
55
56
57
58
59
60

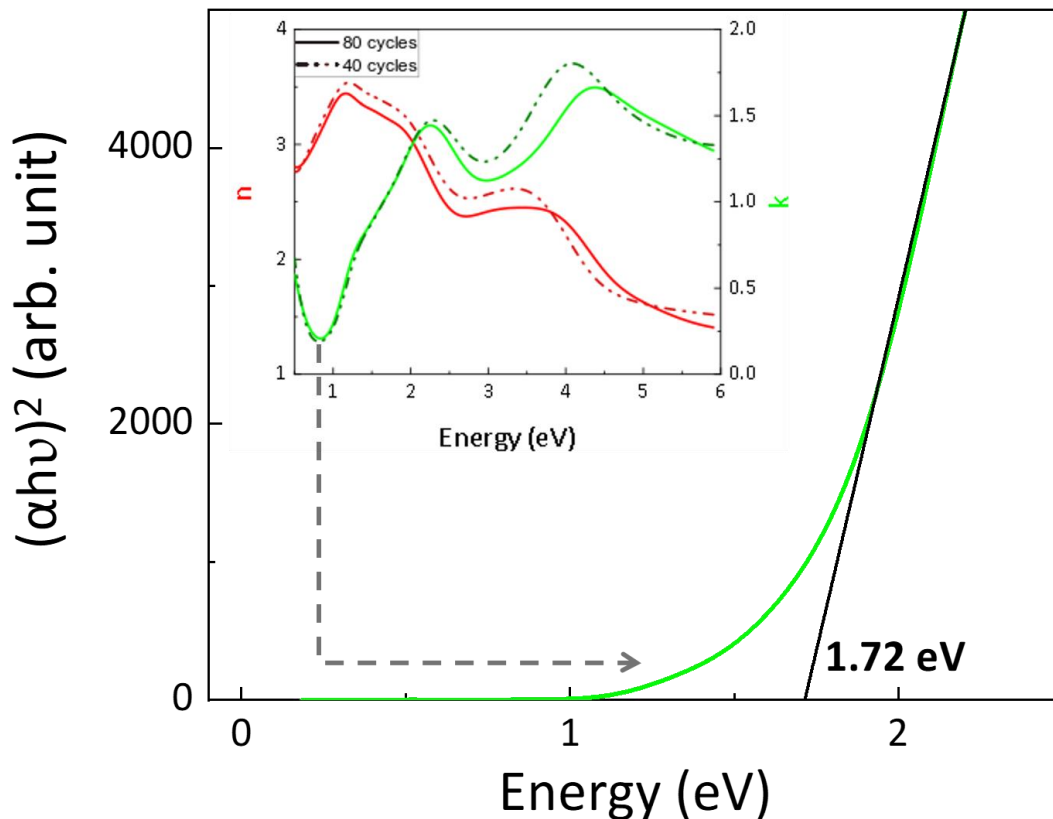


Figure 7: Bandgap identification from the plot of $(\alpha h\nu)^2$ vs the photon energy $h\nu$, showing an estimated direct bandgap of 1.72 eV for a $\text{TiS}_2/100$ nm- SiO_2/Si thin film obtained from 80 ALD/MLD cycles and annealed in $\text{Ar}(96\%)/\text{H}_2(4\%)$ for 30 min at 450°C . The inset shows the optical constants n and k of the complex refractive index as a function of the photon energy, determined by spectroscopic ellipsometry, for thin films obtained from 40 and 80 ALD/MLD cycles and annealed in $\text{Ar}(96\%)/\text{H}_2(4\%)$ for 30 min at 450°C ; n and k are the real and imaginary parts, respectively.

4. Discussion

We report a self-limiting titanium thiolate growth by Atomic Layer Deposition/Molecular Layer Deposition (ALD/MLD) on 100 nm-thick thermally-grown SiO₂ on Si at low temperature (50 °C). From it, lamellar TiS₂ thin films can be obtained by thermal annealing under H₂/Ar at a mild temperature (450 °C, with crystallization starting at even lower temperatures). Organic carbon and (S_n)²⁻ presence show that the annealing is not complete. The films are continuous, smooth, homogeneous, and as thin as 15 nm or even less so. To the best of our knowledge, TiS₂ material has never been obtained with an ALD/MLD approach. The electric measurements on the 15-nm and 30-nm thick thin films show a semiconductor behavior with direct band-gap.

Hereafter some other noteworthy aspects of the process are discussed, namely i) the growth mechanistic insight gained through the modeling studies on silica beads, ii) the growth mechanistic insight gained from *in situ* x-ray studies and comparison with the modeling studies and iii) the preferential orientation of TiS₂ despite the amorphous nature of the substrate.

4.1. *Thiolate growth mechanistic insight on model silica beads*

The development of ALD-grown molecularly-thin layers of MoS₂ on silica-covered silicon wafer was steered by the study of the chemical reactions between the two precursors in absence of substrate and in the presence of high surface area silica beads.²⁵ Herein, we successfully extended this molecular approach for studying the reaction of TDMAT and EDT, *en route* to the targeted ALD/MLD process toward TiS₂.

1
2
3 1
4
56 2 *4.1.1 Reaction between TDMAT and EDT*
7

8
9 3 First of all, the thermodynamically accessible and kinetically facile reaction of
10
11 4 molecular precursors (TDMAT and EDT) among themselves is insightful since it
12
13 5 tends to suggest that an MLD/ALD process targeting TiS_2 and based on their
14
15 6 alternate addition should lead to film growth. However, because of the absence of
16
17 7 a substrate, this reactivity results in coordination polymers which are difficult to
18
19 8 characterize, with no special control over their molecular weight. More importantly
20
21 9 in the context of ALD, the presence of the self-limiting nature of the reaction cannot
22
23 10 be investigated by studying the reactivity of the molecular precursors with each
24
25 11 other.
26
27

28
29 12 *4.1.2 The interest of silica beads*
30

31
32 13 The ALD reaction mechanism was therefore established by investigating the
33
34 14 chemistry occurring at the surface of porous silica nanobeads, as a model for the
35
36 15 flat wafer substrate. The analogy between the 3D surface of silica powders and 2D
37
38 16 surfaces of silica-covered silicon wafer substrates was proposed 25 years ago.⁷³ The
39
40 17 study showed that the ultimate surface of both 2D and 3D substrates are very close
41
42 18 in terms of chemical nature of the reactive sites (silanols, SiO-H), and in terms of
43
44 19 site density as a function of pretreatment temperature. More recently, Surface
45
46 20 OrganoMetallic Chemistry (SOMC) studies⁷⁴ provided titration and reactivity
47
48 21 studies which have further corroborated the validity of this analogy between
49
50 22 pristine flat and porous substrates toward a first metal pulse.^{75–77} The fact that the
51
52 23 density of the anchoring site is proven to be comparable for the two supports tends
53
54 24 to suggest that no different steric hindrance considerations should play for the
55
56
57
58
59
60

1
2
3 1 chemistry occurring on the surface of the silica powder versus the one occurring on
4
5 2 the surface of the silica on the wafer. The diffusion of precursor is surely different
6
7 3 when exposed to a flat surface with respect to a powder; at the same time, the
8
9 4 nature of the (ideal) MLD /ALD process is to be chemistry driven (rather than
10
11 5 diffusion controlled). Therefore, if sufficient precaution is taken to allow the
12
13 6 equilibrium to be reached - and this means long reaction time with the powder in
14
15 7 particular, as is the case in our work - this difference is not anticipated to be
16
17 8 problematic. Furthermore, monitoring with IR allows to have a spectroscopic
18
19 9 handle to gauge *in situ* the change in reaction advancement over time and hence
20
21 10 handle possible diffusion limitations. The main differences between the two
22
23 11 supports remains the overall number of actives sites between the types of
24
25 12 experiments performed (performed on typical scales of hundreds of milligrams of
26
27 13 silica powders having large specific surface area, typically, $200 \text{ m}^2.\text{g}^{-1}$, and much
28
29 14 fewer milligrams of silica of non-porous wafer with geometric surface area of the
30
31 15 order of $10^{-2} \text{ m}^2.\text{g}^{-1}$). It is exactly this significant order of magnitude difference in
32
33 16 favor of the powder that allows to use spectroscopic and analytic tools on the
34
35 17 powder inaccessible to the wafer (see below), and yet, because density is analogous
36
37 18 and diffusion is taken care of, the powder chemistry, with its new molecular-level
38
39 19 insight, has a chance to mimic satisfactorily the chemistry on the wafer. As
40
41 20 mentioned above, our first attempt to use this analogy to model a full ALD process
42
43 21 was successful for growing ultra-thin crystalline MoS_2 nanodomains from
44
45 22 $\text{Mo}(\text{NMe}_2)_4$ and EDT .²⁵
46
47
48
49
50
51 23

1
2
3 1 In the present case, silica-beads model studies demonstrate the successful
4
5 2 chemisorption of both the metal and the sulphur-containing precursors which
6
7 3 ensures mass gain upon each respective ALD or MLD pulse *en route* to TiS₂.
8
9

10 4 4.1.3 Metal pulse mechanism

11
12
13 5 The IR monitoring of the silica beads upon exposure to Ti(NMe₂)₄ pulses and the
14
15 6 connected changes in elemental composition (see **Table 1**) show that titanium
16
17 7 amido bonds in the precursor react with surface sites with concurrent amine
18
19 8 release. This reaction appears complete for the first pulse. The IR spectrum shows
20
21 9 a weak band at 3650 cm⁻¹, distinctive of scant residual surface silanols after the
22
23 10 metal pulse. The titanium loading in **1** of **Scheme 1** (1.7 %w, equivalent to 1.1 Ti/nm²
24
25 11 on the 200m²/g beads used here) is also indicative of a complete coverage, based
26
27 12 on the known concentration of the reactive sites on the starting substrate (ca. 1.15
28
29 13 OH /nm² for silica pre-treated *in vacuo* at 700 °C)⁷⁸.
30
31
32

33 14 In analogy with the established ALD concept of monolayer (ML, fully formed
34
35 15 layer resulting from an ideal ALD cycle) and Growth Per Cycle (GPC, expressed
36
37 16 phenomenologically in nm/cycle or as a fraction of ML/cycle when the ideal ALD
38
39 17 growth mechanism is considered), we can express the chemical data herein by
40
41 18 introducing corresponding concepts such as Chemical Maximum Coverage, CMC,
42
43 19 and Surface Reaction Advancement per Half-Cycle, SRApHC, respectively. These
44
45 20 concepts (CMC and SRApHC) are related yet distinct from ML and GPC since the
46
47 21 latter are defined on the basis of the composition and density of final targeted
48
49 22 phase (TiS₂ here) while the formers are related to the “as deposited” material
50
51 23 (titanium thiolate here). Adopting these distinct metrics could help bridge the gap
52
53
54
55
56
57
58
59
60

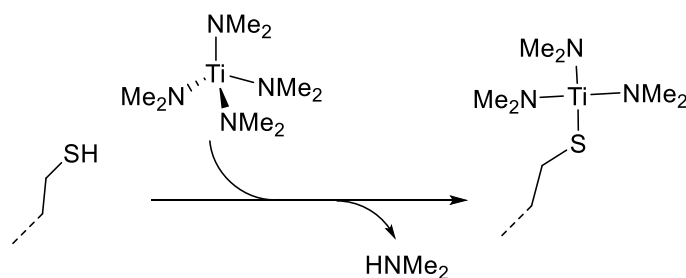
1
2
3 1 between the recurrent hiatus between the (ideal) targeted final phase of the reality
4
5 2 of the “as deposited” material during the ALD process.
6
7

8 3 For the first metal pulse, the combined analyses have suggested a full
9
10 4 coverage, SRApHC (1st Ti-pulse) = 1.0 CMC. During the metal pulse of the second
11
12 5 cycle, the elemental analysis shows an increase of the Ti weight fraction from 1.7%
13
14 6 to 3.0% leading to an approximate atomic composition increase from (surface)-[Ti]₁
15
16 7 to (surface)-[Ti]_{1.7}, showing that there is a substantial yet not complete surface
17
18 8 reaction advancement (70% with respect to the maximum possible for a simple 1:1
19
20 9 stoichiometric growth, *i.e.* SRApHC (2nd Ti-pulse) ≤ 0.7 CMC). During this second
21
22 10 cycle, the other changes in relative molar ratios of the elements that can be
23
24 11 calculated from the elemental analyses similarly show that there is a substantial but
25
26 12 not full surface reaction advancement. Similarly, the empirical formula (see C/Ti,
27
28 13 N/Ti, and S/Ti ratios evolution in **Table 1**) account for the co-existence of newly
29
30 14 metalated surface species and unreacted thiol terminated starting species.
31
32 15 Therefore, only part of the available reactive sites, the thiols SH groups, react with
33
34 16 TDMAT.
35
36
37

38
39 17 During the 6th cycle, the metal content increases after the TDMAT pulse by ca.
40
41 18 10% (from 4.9w% to 5.5w%, see **Table 1**). To a first approximation a complete
42
43 19 coverage during the 6th cycle can be expected to lead to a 20% increase in the value
44
45 20 (from surface-[Ti]₅, to surface-[Ti]₆). Therefore, the titanium loading change during
46
47 21 the metal pulse of the 6th cycle suggests that the surface reaction advancement is
48
49 22 at best 50%, SRApHC (6nd Ti-pulse) ≤ 0.5 CMC.
50
51

52 23 Overall, these changes suggest that during the MLD/ALD step, TDMAT successfully
53
54 24 reacts with the surface thiol groups, by replacement of a titanium amido with a
55
56
57

1 thiolate bond with concurrent amine release (see **Scheme 2** for a proposed generic
 2 average surface reaction scheme for the metal pulse). Only part of the available SH
 3 groups react with TDMAT leading the co-existence of newly metalated surface
 4 species and unreacted thiol terminated starting species, with a concurrent decrease
 5 in surface reaction advancement per half-cycle, SRAPHC along the MLD process, at
 6 least up to the few cycles modelled here. **Scheme 2** reports a proposed generic
 7 average surface reaction scheme for the metal pulse, with an overall decrease in
 8 surface reaction advancement per half-cycle, SRAPHC along the MLD process.



n th ALD Cycle	Molar fraction of ultimate surface composition		Surface Reaction Advancement Per Half-Cycle (SRAPHC) as fraction of Chemical Maximum Coverage (CMC)
2 nd	1	starting amount before metal pulse (a.u)	0
	0.3	final amount after metal pulse (a.u)	0.7
6 th	(1-n)	starting amount before metal pulse (a.u)	n
	(1-n)-0.5	final amount after metal pulse (a.u)	n+0.5

Scheme 2: Proposed general reaction scheme for a metal pulse. The surface reaction advancement per half-cycle, SRAPHC, expressed as fraction of the chemical maximum coverage CMC, calculated from quantitative analytic studies on silica beads models during the 2nd and 6th cycles are reported in the table.

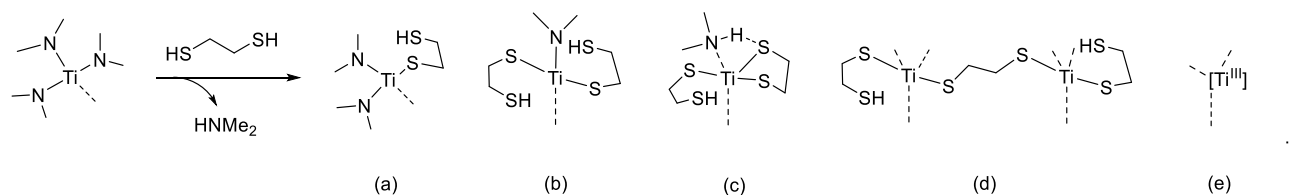
4.1.4 The thiol pulse mechanism

1
2
3 1 The IR monitoring of the silica beads, the analysis of the gas phase and the
4
5 2 connected changes in elemental analyses suggest that EDT reacts, at least partially,
6
7 3 with the Ti-NMe₂ amido moieties present at the surface of the support by
8
9 4 protonolysis, leading to the formation of a Ti-SCH₂CH₂SH thiolate group
10
11 5 concomitantly with release of HNMe₂ in the gas phase. This agrees with literature
12
13 6 in molecular chemistry.⁷⁹

16
17 7 Elemental analysis displayed substantial increase of the S/Ti atomic ratio
18
19 8 (from 1.4 to 4.1 during the EDT pulse of the second cycle), indicating that on average
20
21 9 between one and two EDT ligands (that is between 2 and 4 sulphur atoms) are
22
23 10 added per titanium center. Concurrently, the N/Ti ratio drops but is not nul
24
25 11 suggesting that only part of the available dimethyl-amino-based ligands is
26
27 12 substituted by EDT. Noteworthy, the C/Ti ratio also increases (from 5.3 to 7.2, see
28
29 13 **Table 1**). Simple substitution of -NMe₂ ligand by -SCH₂CH₂SH ligand should not, in
30
31 14 principle, increase the number of carbon atoms (with respect to Ti). Such an
32
33 15 increase may point to incomplete release of -NMe₂ ligands. Consistently, the
34
35 16 observed drop in nitrogen content (N/Ti) is less than the one expected based on
36
37 17 simple amido per thiolate substitution. Protonation of the amido ligand during the
38
39 18 protonolysis exchange reaction with the thiol and coordination of part of the
40
41 19 resulting amine to the metal centre is an explanation consistent with these data.
42
43 20 Proton transfer reactions between thiols and nitrogen-based moieties, (HS-C_n-S)⁻ +
44
45 21 (NMe₂)⁻ → (S-C_n-S)²⁻ + (HNMe₂) (see structure (c) in **Scheme 3**), that has literature
46
47 22 precedents, could also be invoked.^{80,81}

50
51 23 The sulphur-containing solids also EPR active, like the molecular polymer
52
53 24 resulting from mixture of EDT and TDMAT (see **Fig. S4**). The fact that the solid
54
55 25 resulting from EDT addition are EPR active suggests that the reaction between the

1 EDT and TDMAT does not simply imply ligand exchange, as observed for the
 2 molybdenum (IV) analogous system,²⁵ and involves redox activity between the
 3 titanium(IV) precursor and the sulphur-containing ligand, as already observed in
 4 molecular chemistry for several reactions of metal amido complexes with thiols.⁸²
 5 Thiol ligands are known to be reducing agents by -SH coupling.⁸³ While the full
 6 interpretation of these EPR signals goes beyond the scope of this paper, overall,
 7 these EPR data show the presence of redox Ti^{III}/Ti^{IV} surface reactions concomitant
 8 with thiol/amido ligand exchange reactions described above. Therefore, the surface
 9 chemistry goes beyond a simple thiol for amido substitution reaction and entails a
 10 complex set of reactions (see **Scheme 3**).



13 **Scheme 3:** Examples of possible surface reactions occurring during the sulphur pulse of the
 14 process: (a) mono-substitution and (b) bi-substitution of titanium amido ligands by EDT by
 15 protonolysis and release of dimethylamine; concurrent partial (c) proton exchange between thiol
 16 and amido ligands; (d) bridging dithiol substitution and (e) redox reactions leading to titanium(III).

4.1.5 Summary of The MLD mechanism on silica beads

19 In summary, silica-beads model studies demonstrate the successful
 20 chemisorption of both the metal and the sulphur-containing precursors by a self-
 21 limiting growth of a titanium thiolate phase upon each respective ALD or MLD
 22 pulse. The approach proposed here allows having mass gain information *on each*
 23 *element separately*, through elemental analyses, for example, thus offering a well-

1
2
3 1 nuanced description of the surface chemistry occurring at the interface (see
4 **Scheme 2** and **Scheme 3**). This could be an interesting addition to other type of
5
6 2 mechanistic studies in ALD, for example through QCM studies, which can obtain
7
8 3 global, rather than element specific, mass gain at each half pulse to infer the
9
10 4 molecular-level chemical reactions occurring at the gas-solid interface of the
11
12 5 substrate.
13
14 6
15
16
17 7

19 8 **4.2. Thiolate growth mechanistic insight through *in situ* x-ray studies**

22 9 Informed in part by the insightful molecular studies presented above, we
23
24 10 have successfully employed *in situ* x-ray study for assessing the quality of a new
25
26 11 innovative two-step process to TiS₂ thin films on wafers. Both the thiolate growth
27
28 12 and its annealing were studied inside the ALD reactor. The synchrotron brilliance
29
30 13 enabled the study of targeted material growth, under the actual process conditions
31
32 14 and from the first pulse. The possibility to record both the S K_α and Ti K_α
33
34 15 fluorescence yield has allowed us to monitor the S/Ti ratio during the thiolate
35
36 16 growth and during its annealing, the fluorescence yield being directly proportional
37
38 17 to the amount of element deposited on the surface (in the case of ultra-thin films
39
40 18 x-ray absorption is negligible). Over the process, this S/Ti ratio clearly increases. A
41
42 19 similar trend is observed in the molecular studies on silica beads, which proposes
43
44 20 the following molecular explanation: in the early cycles, while less than 1 Ti per S is
45
46 21 added during a metal pulse (see **scheme 2**), between 1 and 2 EDT per Ti are added
47
48 22 during the EDT pulse (**scheme 3**). Another example where directly comparable
49
50 23 insight are accessible for the powder and wafer approaches is given by the observed
51
52 24 partial reduction of Ti(IV) to Ti(III) during the sulfur pulse in both systems. The
53
54
55
56
57
58
59
60

1
2
3 1 presence of S radical signature observed in EPR activity of the layers grown on the
4
5 2 silica-beads correlates to the formation of dithiol moieties identified through the
6
7 3 HAXPES and XPS studies on wafer alongside the presence of Ti(III) center proposed
8
9 4 based on the XANES studies. These similarities corroborate a founding tenet of our
10
11 5 work: that the two systems (powder and wafer) display very similar surface
12
13 6 chemistry.
14
15
16
17 7

18
19 8 X-ray reflectivity data obtained *in situ*, in real time at a fixed angle of reflectivity
20
21 9 allowed to measure the film thickness increase as a function of cycle number (see
22
23 10 **Figure 3(b)**). Each precursor injection leads to a clear jump in thickness which
24
25 11 reaches a constant value during each purge, corroborating the self-limiting surface
26
27 12 chemistry observed by MWE and XRF (see **Figure 3 (a,c,d)**). During the steady
28
29 13 growth regime, the resulting average growth per cycle (GPC) can be estimated as
30
31 14 $0.32 \text{ nm}\cdot\text{cy}^{-1}$. The latter value, agrees with the average GPC value obtained from *in*
32
33 15 *situ* XRR curve measured by varying the incident angle (usual XRR mode), after
34
35 16 deposition of 40-cycles thin film ($0.33 \text{ nm}\cdot\text{cy}^{-1}$, see supporting information **Fig. S10**).
36
37 17 Also, the resolution of the *in situ* XRR at fixed angle of reflectivity during ALD/MLD
38
39 18 study allows to determine the growth per each half-cycle: the thickness gain can be
40
41 19 estimated as $0.18 \text{ nm}\cdot\text{cy}^{-1}$ during TDMAT half-cycle and $0.14 \text{ nm}\cdot\text{cy}^{-1}$ for EDT half-
42
43 20 cycle. As in the silica beads study, the first pulses display markedly different changes
44
45 21 in fluorescence with respect to later ones. This datum is coherent with an expected
46
47 22 increase of the steric hindrance upon film growth (at least in the very early stages).
48
49
50
51
52
53
54
55
56
57
58
59
60

1
2
3 1 The two main approaches explored here, *in situ* synchrotron-based study and
4
5 2 ALD/MLD modeling on large surface area silica beads, appear complementary and
6
7 3 lead to sharply molecularly precise insights in the ALD/MLD process' mechanism on
8
9 4 the wafer. Interestingly, new specific conceptual tools are thus required for this
10
11 5 combination ("real-on wafer" and "model-on powder" ALD/MLD) to be operable,
12
13 6 such as the concept of chemical maximum coverage (CMC) and surface reaction
14
15 7 advancement per half cycle, SRAPHC, introduced in the silica study above and to be
16
17 8 put in echo with the concept of monolayer (ML) and Growth per cycle (GPC) in ALD.
18
19
20

21 9 In summary, the insightful complementarities between the two approaches
22
23 10 comforts in pursuing such tandem approach.
24
25
26
27
28

29 12 **4.3. Preferential TiS₂ orientation parallel to the substrate**

30
31
32 13 The process has achieved nanodomains of crystalline TiS₂ behaving as
33
34 14 semiconductor with direct band-gap with the TiS₂ layers preferentially oriented
35
36 15 parallel to the amorphous substrate surface (SiO₂). Comparison with state-of-the-
37
38 16 art shows that this achievement is a substantial novelty.
39
40

41 17 Thus far, the ALD growth of crystalline TiS₂ layers parallel to the substrate
42
43 18 surface was achieved from TiCl₄ and H₂S precursors only on crystalline substrates
44
45 19 such as ZnS⁷ and the c-sapphire substrate surface², albeit several substrates were
46
47 20 tested, such as sodalime glass, native-SiO₂/Si, ZnS, Rh, Ir, Pd, Pt, Ru, and TiN by Pore
48
49 21 *et al.*⁷, Si(100), stainless steel, c-sapphire and quartz by Sayed *et al.*² and Al₂O₃-
50
51 22 coated native SiO₂ on Si(111) substrate³⁴, carbon paper, or germanium.³⁶
52
53 23 Amorphous TiS₂ or TiS₃ films were obtained when H₂S (at 180°C) was used in
54
55 24 combination with the TDMAT precursor used herein.³⁵ TiS₂ and TiS₃ layers were
56
57
58
59
60

1
2
3 1 also obtained by using both thermal ALD and Plasma Enhanced-ALD from TDMAT.
4
5 2 ³⁸ Post-growing treatment such as rubbing which yields mechanical alignment⁷ or
6
7 3 exposure to sulphur rich atmosphere during post-annealing are worth mentioning
8
9 4 as alternative routes to obtain some alignment crystallization. Noteworthy, the
10
11 5 vertically aligned TiS₂ nanowall network obtained on the c-sapphire substrate
12
13 6 surface grew on top of an amorphous TiS₂, parallel to the film-substrate interface,
14
15 7 along with TiS₂ platelets grown away from the substrate surface.
16
17
18

19 8 This shows that albeit successfully orienting the TiS₂ layers, the C-sapphire
20
21 9 also suffers from non-well-defined initial cycles and concurrent out-of-plane
22
23 10 crystallization which mars the quality of the process, especially if ultra-thin deposits
24
25 11 are targeted. In our case, such ill-defined interphase does not appear to be present
26
27 12 (and is echoed by the homogeneous full-coverage observed on silica beads).
28
29

30 13 In summary, the hybrid ALD/MLD step appears to achieve complete coverage
31
32 14 (1 CMC) of the starting support from the first pulse, based on the results obtained
33
34 15 on the silica bead (the “model” system). We posit that this full coverage occurs also
35
36 16 on the wafer (the “real” system) and contributes to the very thin interlayer between
37
38 17 the support and the final TiS₂ phase observed by TEM on the wafer (see **figure**
39
40 18 **5(c,d)**), and hence contributes to the quality of the final film. The fully amorphous
41
42 19 thiolate phase is then crystallized in a separate step. We posit that the initial lack of
43
44 20 crystalline order is beneficial to the final preferential orientation of the TiS₂
45
46 21 nanodomains since it prevents the coexistence of differently oriented crystallization
47
48 22 seeds before the bulk crystallization temperature is reached. This result
49
50 23 consolidates the pertinence of the two-step approach -first: hybrid ALD/MLD and
51
52 24 second: annealing- presented in the introduction.
53
54
55
56
57
58
59
60

5. Conclusion

In the quest for large-scale deposition methods of 2D TMDC materials, ALD has proven many successes but also limitations, among which the difficulty to produce films with preferential orientation parallel to the substrate, especially if amorphous. We have reported here synthesis strategy alternative to ALD, based on the combination of an ALD metal-pulse (TDMAT) with an organic-precursor MLD pulse (EDT) followed by annealing and applied it to the preparation titanium disulfide (TiS_2). Combining TDMAT and EDT in an ALD/MLD process generates a thin amorphous hybrid organic-inorganic Ti-thiolate material that can be converted into lamellar TiS_2 layers by thermal annealing under $\text{H}_2(4\%)/\text{Ar}(96\%)$ at $450\text{ }^\circ\text{C}$.

Deep understanding and fine control of both steps could be achieved by *in situ* synchrotron XRF, XRD, and XAFS studies during alternating ALD and MLD pulses and annealing steps in a dedicated reactor setup, *ex situ* characterizations for the final phase (NMR, TEM, HAXPES, and Raman scattering), and chemical experimental modeling on high surface area silica beads for the initial cycles of the ALD/MLD process. For this latter study, we have proposed two actionable new parameters, related yet distinct to the established *monolayer* (ML) and *growth-per-cycle* (GPC) parameters used in ALD studies, namely the *chemical maximum coverage* (CMC), and *surface reaction advancement per half-cycle* (SRApHC), as in order to sharpen the description of the chemical reactions occurring at the gas-solid interphase in the MLD/ALD processes, and helping to achieve a performing well-behaved chemical process growth process prepared by hybrid ALD/MLD.

1
2
3 1 The usefulness of strategy followed here, that is decoupling growth from
4
5 2 crystallization, seems well adapted to TMDC and opens new possibilities for the
6
7 3 synthesis of 2D materials in general.
8
9
10 4

11 **Acknowledgments**

12
13
14
15 6 The work was financially supported by the ANR project ANR-18-CE09-0031.
16
17 7 The Ph.D. work of P.A.Y. is financed by the Labex MINOS (ANR-10-LABX-55-01). The
18
19 8 authors acknowledge the facilities and the scientific and technical assistance of the
20
21 9 CMTC characterization platform of Grenoble INP supported by the Centre of
22
23 10 Excellence of Multifunctional Architected Materials (CEMAM) ANR-10-LABX-44-
24
25 11 01 funded by the “Investments for the Future” Program; as well as facilities at the
26
27 12 IRCELYON (UMR 5256 under double tutelage CNRS and Université Claude Bernard
28
29 13 Lyon 1) and CP2M laboratories (UMR 5128, under triple tutelage CNRS, CPE Lyon,
30
31 14 and Université Claude Bernard Lyon 1, into which the former unit C2P2 UMR 5265
32
33 15 where part of this work was carried out merged). The experiment at the SIRIUS
34
35 16 beamline benefited from the SOLEIL beam time allocation no. 20190732. SIRIUS HV
36
37 17 diffractometer was funded by the Swedish Research Council (Vetenskapsrådet MAX
38
39 18 IV–SOLEIL collaboration) and by the Île-de-France region (project ‘FORTE’, DIM
40
41 19 OXYMORE). A part of this work, carried out on the Platform for
42
43 20 Nanocharacterisation (PFNC), was supported by the “Recherche Technologique de
44
45 21 Base” program of the French National Research Agency (ANR). We also
46
47 22 acknowledge the support of the Tandems collaboration project between PHI and
48
49 23 Leti. We acknowledge D. De Barros for ALD reactor engineering assistance and
50
51 24 SERMA technologies for TEM measurements.
52
53
54
55
56
57
58
59
60

1
2
3
4
5
6
7
8
9
10
11
12
13
14
15
16
17
18
19
20
21
22
23
24
25
26
27
28
29
30
31
32
33
34
35
36
37
38
39
40
41
42
43
44
45
46
47
48
49
50
51
52
53
54
55
56
57
58
59
60

1

References

1. Venkata Subbaiah, Y. P., Saji, K. J. & Tiwari, A. Atomically Thin MoS₂ : A Versatile Nongraphene 2D Material . *Adv. Funct. Mater.* **26**, 2046–2069 (2016).
2. Sayed, F. N., Sreedhara, M. B., Soni, A., Bhat, U., Datta, R., Bhattacharyya, A. J., & Rao, C. N. R. Li and Na-ion diffusion and intercalation characteristics in vertically aligned TiS₂ nanowall network grown using atomic layer deposition. *Mater. Res. Express* **6**, (2019).
3. Flamarly-Mespoulie, F., Boulineau, A., Martinez, H., Suchomel, M. R., Delmas, C., Pecquenard, B., & Le Cras, F. Lithium-rich layered titanium sulfides: Cobalt- and Nickel-free high capacity cathode materials for lithium-ion batteries. *Energy Storage Mater.* **26**, 213–222 (2020).
4. Zhang, L., Sun, D., Kang, J., Wang, H. T., Hsieh, S. H., Pong, W. F., ... & Guo, J. Tracking the Chemical and Structural Evolution of the TiS₂ Electrode in the Lithium-Ion Cell Using Operando X-ray Absorption Spectroscopy. *Nano Lett.* **18**, 4506–4515 (2018).
5. Keum, D. H., Cho, S., Kim, J. H., Choe, D. H., Sung, H. J., Kan, M., ... & Lee, Y. H. Bandgap opening in few-layered monoclinic MoTe₂. *Nat. Phys.* **11**, 482–486 (2015).
6. Muller, G. A., Cook, J. B., Kim, H. S., Tolbert, S. H. & Dunn, B. High performance pseudocapacitor based on 2D layered metal chalcogenide nanocrystals. *Nano Lett.* **15**, 1911–1917 (2015).
7. Pore, V., Ritala, M. & Leskelä, M. Atomic layer deposition of titanium disulfide thin films. *Chem. Vap. Depos.* **13**, 163–168 (2007).
8. Harshman, D. R. & Mills, A. P. Concerning the nature of high-T_c superconductivity: Survey of experimental properties and implications for interlayer coupling. *Phys. Rev. B* **45**, 10684–10712 (1992).
9. Wan, C., Kodama, Y., Kondo, M., Sasai, R., Qian, X., Gu, X., ... & Koumoto, K. Dielectric Mismatch Mediates Carrier Mobility in Organic-Intercalated Layered TiS₂. *Nano Lett.* **15**, 6302–6308 (2015).
10. Wu, X. C., Tao, Y. R. & Gao, Q. X. Preparation and field emission properties of titanium polysulfide nanobelt films. *Nano Res.* **2**, 558–564 (2009).

- 1
2
3 1 11. Brune, V., Grosch, M., Weißing, R., Hartl, F., Frank, M., Mishra, S., & Mathur,
4 2 S. Influence of the choice of precursors on the synthesis of two-dimensional
5 3 transition metal dichalcogenides. *Dalt. Trans.* **50**, 12365–12385 (2021).
6
7
- 8 4 12. Hao, S., Zhao, X., Cheng, Q., Xing, Y., Ma, W., Wang, X., ... & Xu, X. A Mini
9 5 Review of the Preparation and Photocatalytic Properties of Two-Dimensional
10 6 Materials. *Front. Chem.* **8**, 1–11 (2020).
11
12
- 13 7 13. George, S. M. Atomic layer deposition: An overview. *Chem. Rev.* **110**, 111–131
14 8 (2010).
15
16
- 17 9 14. Mattinen, M., Leskelä, M. & Ritala, M. Atomic Layer Deposition of 2D Metal
18 10 Dichalcogenides for Electronics, Catalysis, Energy Storage, and Beyond. *Adv.*
19 11 *Mater. Interfaces* **8**, 1–47 (2021).
20
21
- 22 12 15. Cai, J., Han, X., Wang, X. & Meng, X. Atomic Layer Deposition of Two-
23 13 Dimensional Layered Materials: Processes, Growth Mechanisms, and
24 14 Characteristics. *Matter* **2**, 587–630 (2020).
25
26
- 27 15 16. Kim, Y., Woo, W. J., Kim, D., Lee, S., Chung, S. M., Park, J., & Kim, H. Atomic-
28 16 Layer-Deposition-Based 2D Transition Metal Chalcogenides: Synthesis,
29 17 Modulation, and Applications. *Adv. Mater.* **33**, 1–33 (2021).
30
31
- 32 18 17. Park, G. H., Nielsch, K. & Thomas, A. 2D Transition Metal Dichalcogenide Thin
33 19 Films Obtained by Chemical Gas Phase Deposition Techniques. *Adv. Mater.*
34 20 *Interfaces* **6**, 1–31 (2019).
35
36
- 37 21 18. Zhang, H., van Pelt, T., Mehta, A. N., Bender, H., Radu, I., Caymax, M., ... &
38 22 Delabie, A. Nucleation and growth mechanism of 2D SnS₂ by chemical vapor
39 23 deposition: Initial 3D growth followed by 2D lateral growth. *2D Mater.* **5**,
40 24 (2018).
41
42
- 43 25 19. Multia, J. & Karppinen, M. Atomic/Molecular Layer Deposition for Designer's
44 26 Functional Metal–Organic Materials. *Adv. Mater. Interfaces* 2200210 (2022).
45
46
- 47 27 20. Zhao, Y., Zhang, L., Liu, J., Adair, K., Zhao, F., Sun, Y., ... & Sun, X.
48 28 Atomic/molecular layer deposition for energy storage and conversion. *Chem.*
49 29 *Soc. Rev.* **50**, 3889–3956 (2021).
50
51
- 52 30 21. Meng, X. An overview of molecular layer deposition for organic and organic-
53 31 inorganic hybrid materials: Mechanisms, growth characteristics, and
54 32 promising applications. *J. Mater. Chem. A* **5**, 18326–18378 (2017).
55
56
57
58
59
60

- 1
2
3 1 22. Abi Younes, P., Sayegh, S., Nada, A. A., Weber, M., Iatsunskyi, I., Coy, E., ... &
4 2 Bechelany, M. Elaboration of porous alumina nanofibers by electrospinning
5 3 and molecular layer deposition for organic pollutant removal. *Colloids*
6 4 *Surfaces A Physicochem. Eng. Asp.* **628**, 127274 (2021).
7
8
9 5 23. Van de Kerckhove, K., Dendooven, J. & Detavernier, C. Annealing of thin
10 6 "Tincone" films, a tin-based hybrid material deposited by molecular layer
11 7 deposition, in reducing, inert, and oxidizing atmospheres. *J. Vac. Sci. Technol.*
12 8 *A* **36**, 051506 (2018).
13
14
15 9 24. Van de Kerckhove, K., Mattelaer, F., Dendooven, J. & Detavernier, C.
16 10 Molecular layer deposition of "vanadicone", a vanadium-based hybrid
17 11 material, as an electrode for lithium-ion batteries. *Dalt. Trans.* **46**, 4542–4553
18 12 (2017).
19
20
21 13 25. Cadot, S., Renault, O., Frégnaux, M., Rouchon, D., Nolot, E., Szeto, K., ... &
22 14 Quadrelli, E. A. A novel 2-step ALD route to ultra-thin MoS₂ films on SiO₂
23 15 through a surface organometallic intermediate. *Nanoscale* **9**, 467–950 (2016).
24
25
26 16 26. Peters, E. S., Carmalt, C. J. & Parkin, I. P. Dual-source chemical vapour
27 17 deposition of titanium sulfide thin films from tetrakisdimethylamidotitanium
28 18 and sulfur precursors. *Journal of Materials Chemistry* **14**, 3474–3477 (2004).
29
30
31 19 27. Palgrave, R. G. & Parkin, I. P. Chemical vapour deposition of titanium
32 20 chalcogenides and pnictides and tungsten oxide thin films. *New Journal of*
33 21 *Chemistry* **30**, 505–514 (2006).
34
35
36 22 28. Carmalt, C. J., Parkin, I. P. & Peters, E. S. Atmospheric pressure chemical
37 23 vapour deposition of TiS₂ thin films on glass. *Polyhedron* **22**, 1263–1269
38 24 (2003).
39
40
41 25 29. Carmalt, C. J., Neill, S. A. O., Parkin, I. P. & Peters, E. S. Titanium sulfide thin
42 26 films from the aerosol-assisted chemical vapour deposition of [Ti (S-Bu t)₄].
43 27 *Journal of Materials Chemistry* **14**, 830–834 (2004).
44
45
46 28 30. Kanehori, K., Ito, Y., Kirino, F., Miyauchi, K., & Kudo, T. Titanium disulfide films
47 29 fabricated by plasma CVD. *Solid State Ionics* **18**, 818–822 (1986).
48
49
50 30 31. Cheon, J., Gozum, J. E. & Girolami, G. S. Chemical Vapor Deposition of MoS₂
51 31 and TiS₂ Films From the Metal - Organic Precursors Mo (S-t-Bu)₄ and Ti (S-
52 32 t-Bu)₄. *Chemistry of materials* **9**, 1847–1853 (1997).
53
54
55 33 32. Sherrell, P. C., Sharda, K., Grotta, C., Ranalli, J., Sokolikova, M. S., Pesci, F. M.,

- 1
2
3 1 ... & Mattevi, C. Thickness-Dependent Characterization of Chemically
4 2 Exfoliated TiS₂ Nanosheets. *ACS Omega* **3**, 8655–8662 (2018).
5
6
7 3 33. Plashnitsa, V. V., Vietmeyer, F., Petchsang, N., Tongying, P., Kosel, T. H., &
8 4 Kuno, M. Synthetic strategy and structural and optical characterization of thin
9 5 highly crystalline titanium disulfide nanosheets. *J. Phys. Chem. Lett.* **3**, 1554–
10 6 1558 (2012).
11
12
13 7 34. Mahuli, N. & Sarkar, S. K. Atomic layer deposition of titanium sulfide and its
14 8 application in extremely thin absorber solar cells. *J. Vac. Sci. Technol. A*
15 9 *Vacuum, Surfaces, Film.* **33**, 01A150 (2015).
16
17
18 10 35. Nam, H., Yang, H., Kim, E., Bae, C. & Shin, H. Semiconducting TiO_{2-x}S_x thin
19 11 films by atomic layer deposition of TiS₂ and its oxidation in ambient. *J. Vac.*
20 12 *Sci. Technol. A* **37**, 020916 (2019).
21
22
23 13 36. Aljabour, A., Coskun, H., Zheng, X., Kibria, M. G., Strobel, M., Hild, S., ... &
24 14 Stadler, P. Active sulfur sites in semimetallic titanium disulfide enable Co₂
25 15 electroreduction. *ACS Catal.* **10**, 66–72 (2020).
26
27
28 16 37. Zang, X., Shen, C., Kao, E., Warren, R., Zhang, R., Teh, K. S., ... & Lin, L. Titanium
29 17 Disulfide Coated Carbon Nanotube Hybrid Electrodes Enable High Energy
30 18 Density Symmetric Pseudocapacitors. *Adv. Mater.* **30**, (2018).
31
32
33 19 38. Basuvalingam, S. B., Zhang, Y., Bloodgood, M. A., Godiksen, R. H., Curto, A. G.,
34 20 Hofmann, J. P., ... & Bol, A. A. Low-Temperature Phase-Controlled Synthesis
35 21 of Titanium Di- And Tri-sulfide by Atomic Layer Deposition. *Chem. Mater.* **31**,
36 22 9354–9362 (2019).
37
38
39 23 39. Ciatto, G., Chu, M. H., Fontaine, P., Aubert, N., Renevier, H., & Deschanvres, J.
40 24 L. SIRIUS: A new beamline for in situ X-ray diffraction and spectroscopy studies
41 25 of advanced materials and nanostructures at the SOLEIL Synchrotron. *Thin*
42 26 *Solid Films* **617**, 48–54 (2016).
43
44
45 27 40. Boichot, R., Tian, L., Richard, M. I., Crisci, A., Chaker, A., Cantelli, V., ... &
46 28 Renevier, H. Evolution of Crystal Structure During the Initial Stages of ZnO
47 29 Atomic Layer Deposition. *Chemistry of Materials* **28**, 592-600 (2016).
48
49
50 30 41. Skopin, E. V., Abdukayumov, K., Abi Younes, P., Anikin, M., Roussel, H.,
51 31 Deschanvres, J. L., & Renevier, H. In situ ellipsometry monitoring of TiO₂
52 32 atomic layer deposition from Tetrakis (dimethylamido) titanium (IV) and
53 33 H₂O precursors on Si and In_{0.53}Ga_{0.47}As substrates. *Thin Solid Films* **723**,

- 1
2
3 1 1–8 (2021).
4
5
6 2 42. Ciatto, G., Aubert, N., Lecroard, M., Engblom, C., Fontaine, P., Dubuisson, J.
7 3 M., ... & Keller, N. FORTE - a multipurpose high-vacuum diffractometer for
8 4 tender X-ray diffraction and spectroscopy at the SIRIUS beamline of
9 5 Synchrotron SOLEIL. *J. Synchrotron Radiat.* **26**, 1374–1387 (2019).
10
11 6 43. Tanuma, S., Powell, C. J. & Penn, D. R. Calculations of electron inelastic mean
12 7 free paths. IX. Data for 41 elemental solids over the 50 eV to 30 keV range.
13 8 *Surf. Interface Anal.* **43**, 689–713 (2011).
14
15 9 44. Srivastava, J. K., Prasad, M. & Wagner, J. B. Electrical Conductivity of Silicon
16 10 Dioxide Thermally Grown on Silicon. *J. Electrochem. Soc.* **132**, 955 (1985).
17
18 11 45. Singh, A., Li, Y., Fodor, B., Makai, L., Zhou, J., Xu, H., ... & Jaramillo, R. Near-
19 12 infrared optical properties and proposed phase-change usefulness of
20 13 transition metal disulfides. *Appl. Phys. Lett.* **115**, 161902 (2019).
21
22 14 46. Tauc, J. & Menth, A. States in the gap. *J. Non. Cryst. Solids* **8–10**, 569–585
23 15 (1972).
24
25 16 47. Van Doorslaer, S., Shane, J. J., Stoll, S., Schweiger, A., Kranenburg, M., & Meier,
26 17 R. J. Continuous wave and pulse EPR as a tool for the characterization of
27 18 monocyclopentadienyl Ti(III) catalysts. *J. Organomet. Chem.* **634**, 185–192
28 19 (2001).
29
30 20 48. Chu, M. H., Tian, L., Chaker, A., Cantelli, V., Ouled, T., Boichot, R., ... & Ciatto,
31 21 G. An atomistic view of the incipient growth of zinc oxide nanolayers. *Cryst.*
32 22 *Growth Des.* **16**, 5339–5348 (2016).
33
34 23 49. Chu, M. H., Tian, L., Chaker, A., Skopin, E., Cantelli, V., Ouled, T., ... & Ciatto,
35 24 G. Evaluation of Alternative Atomistic Models for the Incipient Growth of ZnO
36 25 by Atomic Layer Deposition. *J. Electron. Mater.* **46**, 3512–3517 (2017).
37
38 26 50. Skopin, E. V., Rapenne, L., Roussel, H., Deschanvres, J. L., Blanquet, E., Ciatto,
39 27 G., ... & Renevier, H. The initial stages of ZnO atomic layer deposition on
40 28 atomically flat In_{0.53}Ga_{0.47}As substrates. *Nanoscale* **10**, 11585–11596
41 29 (2018).
42
43 30 51. Skopin, E. V., Deschanvres, J. L. & Renevier, H. In Situ Ellipsometry Study of the
44 31 Early Stage of ZnO Atomic Layer Deposition on In_{0.53}Ga_{0.47}As. *Phys. Status*
45 32 *Solidi (a)*, **217**, (2020).
46
47
48
49
50
51
52
53
54
55
56
57
58
59
60

- 1
2
3 1 52. Skopin, E. V., Rapenne, L., Deschanvres, J. L., Blanquet, E., Ciatto, G., Pithan,
4 L., ... & Renevier, H. In situ x-ray studies of the incipient ZnO atomic layer
5 2 deposition on In_{0.53}Ga_{0.47}As. *Phys. Rev. Mater.* **4**, 1–9 (2020).
6 3
7
8 4 53. Wu, Z., Ouvrard, G. & Moreau, P. Interpretation of preedge features in the Ti
9 5 and S K-edge x-ray-absorption near-edge spectrain the layered disulfides and.
10 6 *Phys. Rev. B - Condens. Matter Mater. Phys.* **55**, 9508–9513 (1997).
11
12
13 7 54. Brito, J. L., Ilija, M., & Hernández, P. Thermal and reductive decomposition of
14 8 ammonium thiomolybdates. *Thermochimica Acta* **256**, 325-338 (1995).
15
16
17 9 55. Lin, C., Zhu, X., Feng, J., Wu, C., Hu, S., Peng, J., ... & Xie, Y. Hydrogen-
18 10 incorporated TiS₂ ultrathin nanosheets with ultrahigh conductivity for stamp-
19 11 transferrable electrodes. *J. Am. Chem. Soc.* **135**, 5144–5151 (2013).
20
21
22 12 56. Dużyńska, A., Judek, J., Wilczyński, K., Zberecki, K., Łapińska, A., Wróblewska,
23 13 A., & Zdrojek, M. Temperature-induced phonon behavior in titanium disulfide
24 14 (TiS₂) nanosheets. *Journal of Raman Spectroscopy* **50**, 1114–1119 (2019).
25
26
27 15 57. Hangyo, M., Nakashima, S., Hamada, Y., Nishio, T. & Ohno, Y. Raman
28 16 scattering from the misfit-layer compounds SnNbS₃, PbNbS₃, and PbTiS₃.
29 17 *Phys. Rev. B* **48**, 11291–11297 (1993).
30
31
32 18 58. Ishii, M., Saeki, M., & Kawada, I. Raman Study of Non-Stoichiometric Titanium
33 19 Sulfides. *physica status solidi (b)* **124**, K109-K112 (1984).
34
35 20 59. Let, A. L., Mainwaring, D. E., Rix, C. & Murugaraj, P. Thio sol-gel synthesis of
36 21 titanium disulfide thin films and powders using titanium alkoxide precursors.
37 22 *J. Non. Cryst. Solids* **354**, 1801–1807 (2008).
38
39
40 23 60. Let, A. L., Mainwaring, D. E., Rix, C. J. & Murugaraj, P. Thio sol-gel synthesis of
41 24 titanium disulfide thin films and nanoparticles using titanium(IV) alkoxide
42 25 precursors. *J. Phys. Chem. Solids* **68**, 1428–1435 (2007).
43
44
45 26 61. Kasai, H., Tolborg, K., Sist, M., Zhang, J., Hathwar, V. R., Filsø, M. Ø., ... &
46 27 Iversen, B. B. X-ray electron density investigation of chemical bonding in van
47 28 der Waals materials. *Nat. Mater.* **17**, 249–252 (2018).
48
49
50 29 62. Martinez, H., Auriel, C., Gonbeau, D. & Loudet, M. Studies of 1T TiS₂, by STM,
51 30 AFM and XPS: the mechanism of hydrolysis in air. *Applied surface science* **93**,
52 31 0–4 (1996).
53
54
55 32 63. Fulghum, J. E. Determination of overlayer thickness by angle-resolved XPS: A
56
57
58
59
60

- 1
2
3
4 1 comparison of algorithms. *Surf. Interface Anal.* **20**, 161–173 (1993).
- 5
6 2 64. Dupin, J. C., Gonbeau, D., Martin-Litas, I., Vinatier, P. & Levasseur, A.
7 3 Amorphous oxysulfide thin films MO_yS_z (M = W, Mo, Ti) XPS characterization:
8 4 Structural and electronic peculiarities. *Applied Surface Science* **173**, 140–150
9 5 (2001).
- 10
11
12 6 65. Lindic, M. H., Martinez, H., Benayad, A., Pecquenard, B., Vinatier, P.,
13 7 Levasseur, A., & Gonbeau, D. XPS investigations of TiO_yS_z amorphous thin
14 8 films used as positive electrode in lithium microbatteries. *Solid State Ionics*
15 9 **176**, 1529–1537 (2005).
- 16
17
18 10 66. Lindic, M. H., Pecquenard, B., Vinatier, P., Levasseur, A., Martinez, H.,
19 11 Gonbeau, D., ... & Ouvrard, G. Characterization of rf sputtered TiO_yS_z thin
20 12 films. *Thin Solid Films* **484**, 113–123 (2005).
- 21
22
23 13 67. Dubois, V., Pecquenard, B., Soule, S., Martinez, H. & Le Cras, F. Dual cation-
24 14 and anion-based redox process in lithium titanium oxysulfide thin film
25 15 cathodes for all-solid-state lithium-ion batteries. *ACS Appl. Mater. Interfaces*
26 16 **9**, 2375–2384 (2017).
- 27
28
29 17 68. Richard, J., Benayad, A. & Martinet, S. Charge Transfer Mechanism into the
30 18 Chevrel Phase Mo₆S₈ during Mg Intercalation. *The Journal of Physical*
31 19 *Chemistry C* **121**, 17096-17103 (2017).
- 32
33
34 20 69. Martinez, H., Benayad, A., Gonbeau, D., Vinatier, P., Pecquenard, B., &
35 21 Levasseur, A. Influence of the cation nature of high sulfur content oxysulfide
36 22 thin films MO_yS_z (M = W, Ti) studied by XPS. *Appl. Surf. Sci.* **236**, 377–386
37 23 (2004).
- 38
39
40 24 70. Gonbeau, D., Guimon, C., Pfister-Guillouzo, G., Levasseur, A., Meunier, G., &
41 25 Dormoy, R. XPS study of thin films of titanium oxysulfides. *Surf. Sci.* **254**, 81–
42 26 89 (1991).
- 43
44
45 27 71. Verner, D. A., Ferland, G. J., Korista, K. T. & Yakovlev, D. G. Atomic Data for
46 28 Astrophysics. II. New Analytic FITS for Photoionization Cross Sections of Atoms
47 29 and Ions. *Astrophys. J.* **465**, 487 (1996).
- 48
49
50 30 72. Liu, Y., Porter, S. H. & Goldberger, J. E. Dimensional Reduction of a Layered
51 31 Metal Chalcogenide into a 1D Near-IR Direct Band Gap Semiconductor. *J. Am.*
52 32 *Chem. Soc.* **134**, 5044-5047 (2012).
- 53
54
55 33 73. Sneh, O. & George, S. M. Thermal stability of hydroxyl groups on a well-

- 1
2
3 1 defined silica surface. *J. Phys. Chem.* **99**, 4639–4647 (1995).
4
5 2 74. Coperet, C., Comas-Vives, A., Conley, M. P., Estes, D. P., Fedorov, A., Mougel,
6 3 V., ... & Zhizhko, P. A. Surface Organometallic and Coordination Chemistry
7 4 toward Single-Site Heterogeneous Catalysts: Strategies, Methods, Structures,
8 5 and Activities. *Chem. Rev.* **116**, 323–421 (2016).
9
10 6 75. Roussey, A., Gentile, P., Lafond, D., Martinez, E., Jousseume, V., Thieuleux,
11 7 C., & Copéret, C. Cu nanoparticles on 2D and 3D silica substrates: Controlled
12 8 size and density, and critical size in catalytic silicon nanowire growth. *J. Mater.*
13 9 *Chem. C* **1**, 1583–1587 (2013).
14
15 10 76. Mathey, L., Alphazan, T., Valla, M., Veyre, L., Fontaine, H., Enyedi, V., ... &
16 11 Copéret, C. Functionalization of silica nanoparticles and native silicon oxide
17 12 with tailored boron-molecular precursors for efficient and predictive p-doping
18 13 of silicon. *J. Phys. Chem. C* **119**, 13750–13757 (2015).
19
20 14 77. Alphazan, T., Mathey, L., Schwarzwald, M., Lin, T. H., Rossini, A. J., Wischert,
21 15 R., ... & Copéret, C. Monolayer Doping of Silicon through Grafting a Tailored
22 16 Molecular Phosphorus Precursor onto Oxide-Passivated Silicon Surfaces.
23 17 *Chem. Mater.* **28**, 3634–3640 (2016).
24
25 18 78. Zhuravlev, L. T. The surface chemistry of amorphous silica . Zhuravlev model.
26 19 *Colloids and Surfaces A: Physicochemical and Engineering Aspects* **173**, 1–38
27 20 (2000).
28
29 21 79. Diamond, G. M., Jordan, R. F. & Petersen, J. L. Synthesis of group 4 metal rac-
30 22 (EBI)M(NR₂)₂ complexes by amine elimination. Scope and limitations.
31 23 *Organometallics* **15**, 4030–4037 (1996).
32
33 24 80. Bachrach, S. M., Nguyen, T. T. & Demoin, D. W. Microsolvation of cysteine: A
34 25 density functional theory study. *J. Phys. Chem. A* **113**, 6172–6181 (2009).
35
36 26 81. Ataman, E., Isvoranu, C., Andersen, J. N., Schnadt, J. & Schulte, K.
37 27 Unconventional zwitterionic state of l-cysteine. *J. Phys. Chem. Lett.* **2**, 1677–
38 28 1681 (2011).
39
40 29 82. Mukherjee, A., Sengupta, S. K., Steeves, D. M., Soares, J. W. & Whitten, J. E.
41 30 Mechanism of thiol-induced color change of tungsten oxide nanoparticles.
42 31 *Chem. Phys. Lett.* **752**, (2020).
43
44 32 83. Wang, M. & Jiang, X. Sulfur–Sulfur Bond Construction. *Top. Curr. Chem.* **376**,
45 33 14 (2018).
46
47
48
49
50
51
52
53
54
55
56
57
58
59
60

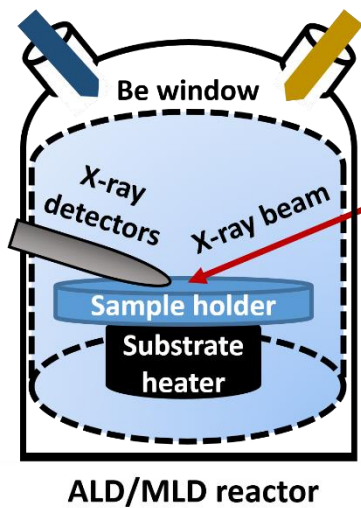
1
2
3
4
5
6
7
8
9
10
11
12
13
14
15
16
17
18
19
20
21
22
23
24
25
26
27
28
29
30
31
32
33
34
35
36
37
38
39
40
41
42
43
44
45
46
47
48
49
50
51
52
53
54
55
56
57
58
59
60

1

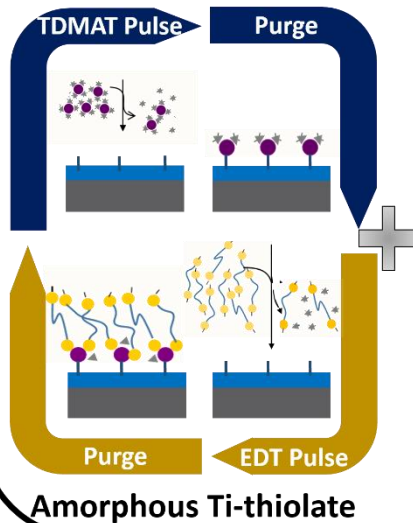
2

Graphical abstract

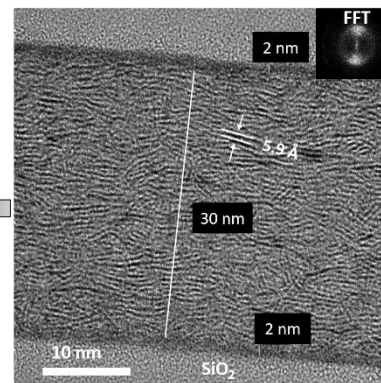
In situ x-ray studies



ALD/MLD cycle



Thermal annealing



TiS₂ thin film

3